Chemical Engineering Journal 533 (2026) 174635

Contents lists available at ScienceDirect

Chemical Engineering Journal

journal homepage: www.elsevier.com/locate/cej

Support-dependent charge transfer and ROS pathways in Pt/g-C_3N_4 and Pt/TiO_2 photocatalysts

Gregor Žerjav [a,*], Andraž Mavrič [b], Miklós Németh [c], Albin Pintar [a]

[a] Department of Inorganic Chemistry and Technology, National Institute of Chemistry, Hajdrihova ulica 19, SI-1001, Ljubljana, Slovenia
[b] Materials Research Laboratory, University of Nova Gorica, Vipavska 13, SI-5000, Nova Gorica, Slovenia
[c] HUN-REN Centre for Energy Research, Institute for Energy Security and Environmental Safety, Department of Surface Chemistry and Catalysis, Konkoly-Thege M. street 29-33, H-1121, Budapest, Hungary

ARTICLE INFO

Keywords:
Environmental photocatalysis
Bisphenol A degradation
NO_2 removal
Pt-loaded semiconductors
Visible-light activation
g-C_3N_4
TiO_2

ABSTRACT

Understanding how platinum cocatalysts interact with semiconductor supports remains a central challenge in photocatalysis. Although Pt nanoparticles are often assumed to act as a universal electron sink, this study demonstrates that their catalytic behaviour is governed by the electronic structure, defect chemistry, and interfacial energetics of the support. To isolate support-induced effects, TiO_2 nanorods (S_{BET} = 93.3 m^2 g^{-1}) and two texturally distinct forms of g-C_3N_4 (a low-surface-area CN-L (20 m^2 g^{-1}) and a high-surface-area CN-H (85.0 m^2 g^{-1})) deliberately matched to TiO_2 were modified with identical 1 wt% Pt nanoparticles using the same impregnation-reduction protocol. Despite comparable surface areas for TiO_2 and CN-H, Pt-modified catalysts exhibit fundamentally different interfacial energetics and charge-transfer behaviour. TiO_2 stabilizes highly metallic Pt nanoparticles (~1.0 nm) and forms a very low Schottky barrier (0.16 eV), enabling rapid electron extraction and pronounced Pt-mediated visible-light ROS generation. In contrast, g-C_3N_4 induces strong band bending and stabilizes mixed Pt^0/Pt^{2+} states, resulting in higher interfacial barriers (0.26–1.19 eV), suppressed hydroxyl radical formation, and enhanced selective one-electron oxidation, more than doubling ABTS generation compared to pristine CN-L. These electronic effects translate directly into photocatalytic performance. TiO_2@Pt exhibits efficient visible-light BPA degradation and the lowest NO_2 reduction onset temperature, while CN-H@Pt outperforms CN-L@Pt due to improved charge separation and approximately 40% lower charge-transfer resistance. The persistence of these contrasts between TiO_2@Pt and CN-H@Pt confirms that Pt nanoparticles functionality is electronically programmed by the support rather than dictated by surface accessibility. This insight provides a rational framework for engineering noble-metal photocatalysts through deliberate control of semiconductor electronic structure and interfacial chemistry.

1. Introduction

Environmental pollution continues to escalate as one of the most persistent global threats, driven by the steady accumulation of organic contaminants, pharmaceutical residues, endocrine-disrupting compounds, and reactive nitrogen species such as NO_x in natural water and air systems [1–3]. These pollutants resist natural degradation and pose substantial hazards to human health, ecological stability, and long-term biodiversity. Conventional remediation approaches, including thermal oxidation, adsorption, advanced oxidation processes, and biological treatment, have significant drawbacks such as high energy consumption, limited mineralization efficiency, and the generation of secondary waste streams [4]. Consequently, there is an urgent need for clean, low-energy, solar-driven technologies capable of degrading pollutants under mild conditions.

Semiconductor-based photocatalysis has emerged as a highly promising solution to this challenge [5]. Its ability to harness sunlight or visible-light to activate semiconductor surfaces and generate highly reactive oxygen species (ROS) makes it particularly suitable for sustainable environmental purification. Over the past two decades, materials such as titanium dioxide (TiO_2) [6], graphitic carbon nitride (g-C_3N_4) [7], ZnO [8], WO3 [9], and various metal sulphides [10] have been widely investigated for their favourable band structures, tunable optical properties, and chemical robustness. However, the intrinsic

* Corresponding author.
E-mail address: gregor.zerjav@ki.si (G. Žerjav).

https://doi.org/10.1016/j.cej.2026.174635
Received 16 January 2026; Received in revised form 12 February 2026; Accepted 24 February 2026
Available online 25 February 2026

recombination of photogenerated charge carriers in these materials remains the primary factor limiting their photocatalytic performance, as it suppresses both charge utilization efficiency and ROS generation pathways. To mitigate recombination losses and enhance ROS production, hybrid photocatalysts incorporating noble metals or secondary semiconductors have been extensively explored [11–14]. Noble metals nanoparticles (NPs) such as Pt [15,16], Au [17], and Ag [18] can act as electron sinks, plasmonic light absorbers, and surface catalytic centers. Among them, Pt NPs are traditionally regarded as the most versatile cocatalyst due to its ability to form efficient Schottky junctions, accelerate charge extraction, lower reaction activation barriers, and stabilize key ROS intermediates [19]. As a result, Pt-based hybrid photocatalysts are frequently assumed to share common mechanistic features, irrespective of the semiconductor support to which Pt is anchored. Yet, emerging evidence suggests that this assumption is oversimplified and potentially misleading. In fact, the behaviour of Pt NPs, such as partial oxidation, electronic structure, electron trapping capacity, interaction with defects, and ability to mediate ROS formation, can vary dramatically depending on the underlying semiconductor. This implies that the support itself may be the primary determinant of Pt NPs functionalities, rather than Pt NPs acting as a universal, support-invariant cocatalyst. Surprisingly, this critical question remains largely unexplored due to the lack of rigorous, controlled comparative studies.

Among the broad family of photocatalysts, TiO_2 and g-C_3N_4 represent two particularly insightful "model" semiconductors for probing support-governed Pt NPs behaviour. TiO_2 is a rigid, wide-band-gap oxide with a well-defined electronic structure, deep valence states, and stable surface chemistry [12]. Pt NPs on TiO_2 typically form classical Schottky junctions that facilitate ultrafast electron trapping [20]. In contrast, g-C_3N_4 is a visible-light-active, metal-free, polymeric semiconductor with a nitrogen-rich π-conjugated network capable of stabilizing oxidized metal species, providing abundant lone-pair surface functionalities, and exhibiting high defect tolerance [21,22]. Its conduction band is significantly more negative than that of TiO_2, favouring superoxide anion radical generation over hydroxyl radical formation [23]. Additionally, while TiO_2 generally possesses high specific surface area and well-defined meso- or nanostructures, g-C_3N_4 typically exhibits much lower surface area and more complex porosity, unless specially engineered [24–26]. These inherent differences mean that Pt nanoparticles deposited on TiO_2 or g-C_3N_4 are expected to experience entirely different electronic environments, interfacial charge-transfer dynamics, and ROS formation mechanisms. Yet, determining the extent to which Pt NPs behaviour is governed by these support-specific properties has been severely hindered by methodological limitations in the literature. Most comparative studies use materials with vastly different surface areas, morphologies, or Pt NPs deposition protocols, making it impossible to isolate electronic effects of the support from geometric or synthetic artefacts.

The novelty of this study lies in directly addressing these limitations by constructing TiO_2 and g-C_3N_4 supports with comparable mesoporous textural properties and loading them with Pt NPs using an identical impregnation-reduction synthesis. This careful design provides a rare and highly controlled platform in which differences in Pt oxidation state, dispersion, charge-transfer behaviour, and ROS formation can be attributed unequivocally to the electronic and chemical nature of the support, rather than to differences in exposed surface area or deposition chemistry. In this work, g-C_3N_4 was synthesized in two distinct textural forms: a low-surface-area variant (CN-L, 20 $m^2\ g^{-1}$) and a high-surface-area analogue (CN-H, 85.0 $m^2\ g^{-1}$), while TiO_2 nanorods with a comparable accessible surface area (93.3 $m^2\ g^{-1}$) to CN-H were synthesized in-house. All three supports were modified with an identical Pt loading (1 wt%) using the same synthesis protocol, ensuring equivalent conditions for Pt precursor adsorption, reduction, and nanoparticle growth. This methodological consistency eliminates synthetic bias and allows direct evaluation of how band alignment, defect chemistry, surface functionalities, and structural order govern Pt behaviour. To elucidate these relationships, we use a comprehensive suite of characterization methods, including XPS valence-band analysis, UV–Vis diffuse reflectance spectroscopy, steady-state photoluminescence, time-resolved TCSPC, and solid-state EPR spectroscopy. These complementary techniques enable us to resolve the interfacial electronic structure with high precision and correlate it with photocatalytic reactivity, charge-carrier dynamics, and ROS formation pathways. Through this integrated approach, we show that the catalytic role of Pt NPs is not universal but is profoundly dictated by the underlying semiconductor, which controls Pt oxidation state, electron-extraction efficiency, defect interactions, and radical-species selectivity. The insights gained here establish a rigorous foundation for the rational design of next-generation Pt-based photocatalysts with optimized interfacial architectures and tailored ROS-driven activity.

2. Experimental

2.1. Catalyst synthesis

Ultra-pure water (18.2 MΩ·cm) was used in all procedures, and all chemicals were of analytical grade and used without further purification. Graphitic carbon nitride (g-C_3N_4) was synthesized by calcining dicyandiamide (DCDA, Sigma-Aldrich) in a covered alumina crucible using a muffle furnace (Nabertherm, Germany, model LT 9/11/SKM). For the low-surface-area sample (CN-L), the temperature was raised to 550 °C at 300 °C·h^{-1} and held for 4 h, while for the high-surface-area sample (CN-H), the temperature was increased to 642 °C at 225 °C·h^{-1} and held for 3.33 h. TiO_2 nanorods (denoted as TiO_2) were prepared hydrothermally by dispersing 2 g of TiO_2 precursor (DT-51, CristalACTiV™) in 10 M NaOH solution, heating the mixture at 130 °C for 24 h in a Teflon-lined autoclave, washing the product with 0.1 M HCl and ultra-pure water, and calcining it at 500 °C for 2 h (120 °C·h^{-1}). Platinum was deposited on CN-L, CN-H, and TiO_2 supports by wet impregnation using a diamminedinitritoplatinum(II) precursor (Sigma-Aldrich, 3.4 wt% Pt in NH_3 solution) to achieve 1 wt% Pt loading. Each support (0.5 g) was dispersed in 250 mL of absolute ethanol, ultrasonicated for 10 min, mixed with 0.25 mL of the Pt precursor solution for 120 min, and the solvent was removed by rotary evaporation (Büchi, model R-215). The pH of the impregnation suspensions was measured and was 8 for all supports. The solids were dried at 80 °C for 20 h and reduced under forming gas (5% H_2 in N_2, Linde) at 300 °C for 2 h (150 °C·h^{-1}) in a tubular quartz furnace (Carbolite). The resulting catalysts were denoted CN-L@Pt, CN-H@Pt, and TiO_2@Pt. A nominal Pt loading of 1 wt% was selected as a widely adopted benchmark in Pt-modified photocatalysts, providing sufficient Pt density for reliable spectroscopic and electrochemical characterization while minimizing particle growth and preserving strong metal-support interactions. Importantly, the aim of this work is not to optimise Pt loading, but to enable an isolated comparison of support-governed Pt electronic structure and ROS selectivity under identical Pt deposition conditions.

2.2. Experimental methods

Comprehensive descriptions of all analytical and photocatalytic procedures used in this work are provided in the Supplementary information. The Supplementary information includes full instrumental settings and operational parameters for X-ray diffraction (XRD), attenuated total reflectance Fourier-transform infrared spectroscopy (ATR-FTIR), nitrogen physisorption analysis (Brunauer-Emmett-Teller and Barrett-Joyner-Halenda; BET/BJH), scanning electron microscopy with energy-dispersive X-ray spectroscopy (SEM-EDX), ultraviolet-visible diffuse reflectance spectroscopy (UV–Vis DRS), steady-state photoluminescence (PL), time-correlated single-photon counting (TCSPC), and X-ray photoelectron spectroscopy (XPS), including valence band analysis. ATR-FTIR spectroscopy was used to examine the chemical bonding and framework integrity of the supports, while the crystalline

lattice structure and phase composition were determined solely by X-ray diffraction (XRD) and electron microscopy. Experimental details for solid-state electron paramagnetic resonance (EPR) measurements performed in the dark and under visible-light irradiation are also included. Complete photocatalytic procedures for water-dissolved bisphenol A (BPA) degradation, reactive oxygen species (ROS) detection assays, and nitrogen dioxide (NO_2) removal, covering reactor configuration, illumination conditions, analytical quantification, and kinetic evaluation, are provided in the Supplementary information. The spectral power distributions of all illumination sources used in the experiments are shown in Fig. S1.

3. Results and discussion

3.1. Structural and textural properties of catalysts

The diffraction patterns of the synthesized materials (Fig. 1) confirm the formation of polymeric g-C_3N_4 and anatase TiO_2. The CN-L and CN-H samples display typical g-C_3N_4 diffraction features, including a broad (002) stacking reflection at approximately 27.4° and a weaker (100)

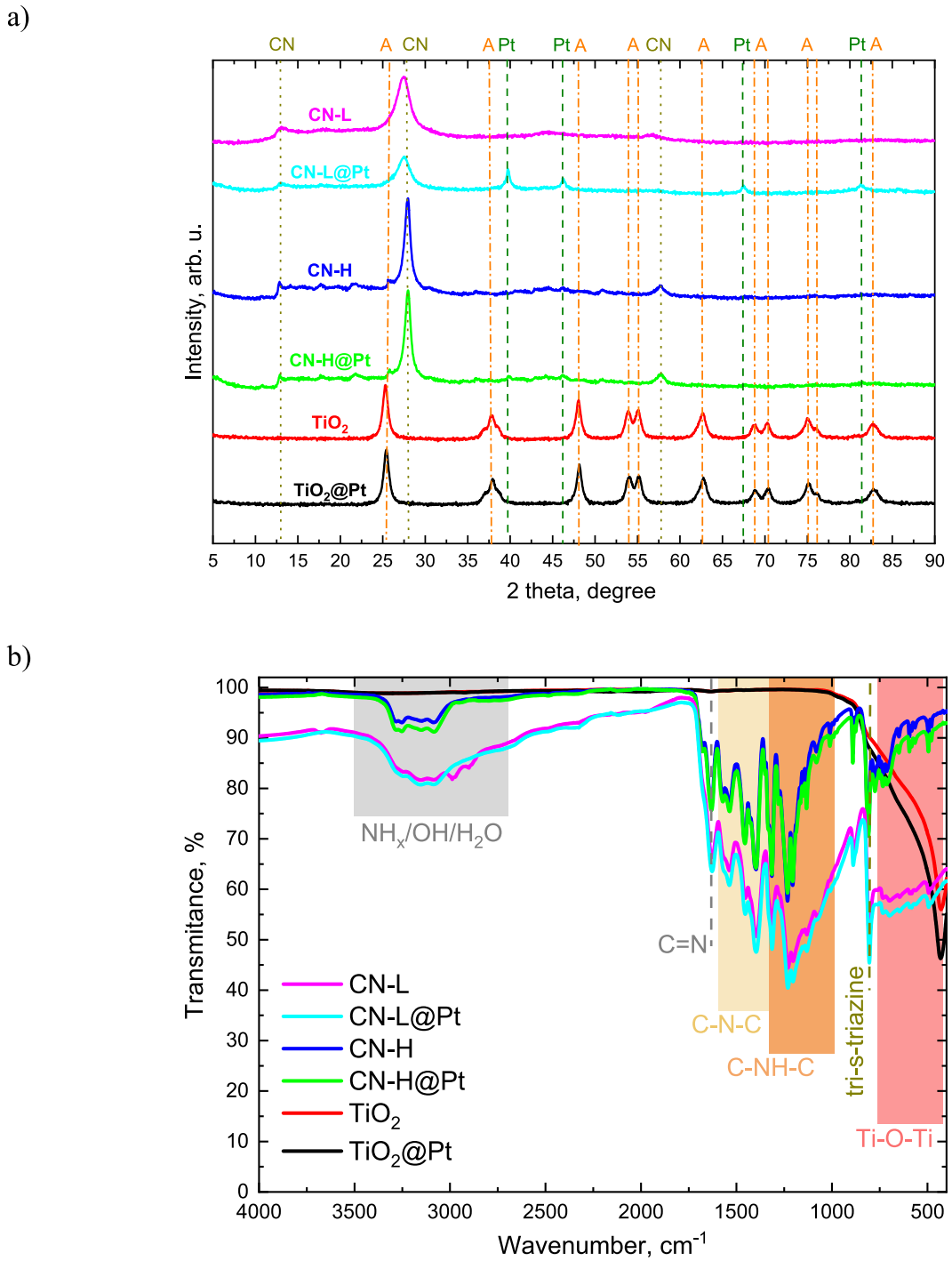

Fig. 1. a) XRD patterns of the investigated photocatalysts. Orange dashed lines indicate the characteristic reflections of anatase TiO_2 (PDF 01-086-1157), grey dashed lines correspond to g-C_3N_4 (PDF 00-066-0813), and green dashed lines denote the reflections of metallic Pt (PDF 04-001-0537). b) ATR-FTIR spectra of the analyzed nanosolids, recorded at room temperature, with inset to highlight the characteristic vibrational modes of g-C_3N_4 and TiO_2.

peak at around 13°, consistent with a layered heptazine-based structure. The crystallite size estimated from the (002) reflection is 8.0 nm for CN-L and 18.0 nm for CN-H (Table 1), indicating a substantially higher degree of structural order in the high-surface-area material. Pt deposition does not alter the position or width of the g-C_3N_4 reflections, demonstrating that the polymeric framework remains intact. However, the high-angle region in Fig. S2 (2θ = 38–84°) shows several well-defined reflections at 39.7°, 46.1°, 67.5°, and 81.2°, corresponding to the (111), (200), (220), and (311) planes of metallic Pt (PDF 04-001-0537). These peaks are clearly visible in both CN-L@Pt and CN-H@Pt, confirming the formation of crystalline Pt^0 nanoparticles. Their intensity is highest for CN-L@Pt, which is consistent with the lower surface area and smaller number of nucleation sites on CN-L, favouring the growth of larger Pt crystallites. Conversely, CN-H@Pt shows the same Pt reflections but with broader and less intense features, indicating smaller Pt domains formed on the highly porous CN-H surface. The TiO_2 pattern displays sharp reflections characteristic of well-crystallized anatase, with an average crystallite size of 25 nm (Table 1). Pt loading does not induce detectable changes in the TiO_2 diffraction profile, and no distinct Pt reflections appear in the TiO_2@Pt diffractogram. This can be attributed to two factors: (i) the strong and highly crystalline anatase background, which masks low-intensity Pt peaks, and (ii) the formation of very small and highly dispersed Pt nanoparticles on TiO_2, whose crystallite size falls below the detection limit of laboratory XRD [27]. Overall, the XRD analysis shows that Pt nanoparticles are detectable on g-C_3N_4 due to its weaker diffraction background and smaller crystallite domains (8–18 nm), while the highly crystalline TiO_2 (25 nm) obscures Pt signals despite the presence of metallic Pt.

The ATR-FTIR spectra of the investigated materials (Fig. 1b) show the characteristic vibrational features of polymeric g-C_3N_4 and anatase TiO_2, confirming the successful synthesis of both supports and the preservation of their structures after Pt deposition. All carbon nitride samples (CN-L, CN-H, and their Pt-modified counterparts) display a series of strong absorption bands between 1200 and 1650 cm^{-1}, corresponding to C—N and C═N stretching modes within heptazine units [28–30]. The broad envelope in this region reflects the superposition of multiple vibrations associated with the tri-*s*-triazine framework [28,30]. A distinct band at 805 cm^{-1} is observed for all CN materials and is assigned to the breathing mode of the heptazine ring, serving as a fingerprint feature of g-C_3N_4 [29]. In the high-wavenumber region, a broad feature between 3000 and 3400 cm^{-1} is visible, arising from N—H and O—H stretching vibrations from surface amine groups and adsorbed water [31]. The relative intensity of this band is slightly higher in CN-L and CN-L@Pt, consistent with their lower degree of surface condensation. Importantly, clear differences between CN-L and CN-H are also observed in the heptazine-related region: CN-L shows broader, less resolved C–N/C=N stretching bands and a more pronounced N–H/O–H signal, indicating a less ordered, more defect-rich framework with a higher density of terminal -NH_x groups. In contrast, CN-H displays sharper, better-defined vibrations, consistent with its larger crystallite size, higher structural condensation, and overall improved heptazine ordering. The TiO_2 samples exhibit the typical Ti–O–Ti lattice vibrations in the 400–800 cm^{-1} region, with a prominent band centered near 500 cm^{-1}, characteristic of anatase [32]. The spectra of TiO_2 and TiO_2@Pt are nearly identical, indicating that Pt deposition does not perturb the TiO_2 lattice or introduce new IR-active species. The overall similarity of the CN-L and CN-H spectra before and after Pt addition further indicates that the heptazine framework remains intact and that Pt nanoparticles do not alter the chemical structure of g-C_3N_4.

The N_2 adsorption-desorption isotherms (Fig. S3a) reveal clear textural differences among the investigated photocatalysts. Both CN-L and CN-L@Pt exhibit low uptake across the entire relative pressure range, reflecting their limited porosity and low surface areas (19.0 and 17.6 $m^2\ g^{-1}$, respectively; Table 1). Their isotherms resemble a type II profile with very weak H3-type hysteresis, characteristic of largely non-porous or weakly mesoporous carbon nitride structures [33]. In contrast, CN-H and CN-H@Pt display markedly higher N_2 adsorption, consistent with their significantly larger surface areas (85.0 and 81.0 $m^2\ g^{-1}$). The broader hysteresis loop at medium to high relative pressures indicates the presence of slit-shaped mesopores, originating from the more open and better-condensed polymeric network. The minor decrease in surface area after Pt deposition confirms that Pt NPs do not obstruct the pore structure of g-C_3N_4. TiO_2 and TiO_2@Pt exhibit the highest adsorption capacities among all samples, characteristic of their high-surface-area nanorod morphology (93.3 and 91.9 $m^2\ g^{-1}$). The steep N_2 uptake near $p/p^0 \rightarrow 1$ is typical of interparticle mesoporosity created by the rod-like architecture. Pt loading does not affect the isotherm shape, indicating that the nanorod assembly remains unchanged. The BJH pore-size distribution curves (Fig. S3b) further support these observations. CN-L shows a broad and weak distribution of pores greater than 10 nm, consistent with structural voids rather than well-defined mesoporosity. CN-H displays a more pronounced mesopore population centered around 10 to15 nm, reflecting its better-developed pore network. TiO_2 samples exhibit a sharp and intense pore distribution with a maximum around 15 to 20 nm, characteristic of uniform mesopores formed between aggregated nanorods. Overall, these results demonstrate that CN-H possesses a much more developed mesoporous structure than CN-L, while TiO_2 exhibits the largest accessible surface area and well-defined mesoporosity. The minimal differences between bare and Pt-loaded samples confirm that Pt deposition does not significantly alter the intrinsic textural properties of any support.

The SEM micrographs (Fig. S4) provide detailed insight into the morphological characteristics of the synthesized photocatalysts. The CN-L and CN-H samples both display the typical layered morphology of polymeric g-C_3N_4, but with clear differences in structural development. CN-L consists of dense, compact agglomerates composed of thick, irregular layered domains with limited interlayer separation, consistent with its low surface area and lower degree of structural condensation. In contrast, CN-H displays a more open, thin, sheet-like morphology, characterized by loosely stacked and partially exfoliated layered g-C_3N_4

Table 1
Listed are the specific surface area (S_{BET}), total pore volume (V_{pore}), average pore diameter (d_{pore}), crystallite size of anatase TiO_2 at 25° and g-C_3N_4 at 27° (a.c.s.), optical band gap (*Eg*) determined using the Kubelka-Munk function, valence band maximum (VB), conduction band position (CB), Schottky barrier height (SBH), and values of the R_{CT} obtained by mean of EIS measurements.

	S_{BET}	V_{pore}	d_{pore}	a.c.s.	VB	*Eg*	CB[a]	SBH[b]	R_{CT}	R_{CT}[c]
	$m^2\ g^{-1}$	$cm^3\ g^{-1}$	nm		eV				MΩ	
CN-L	19.0	0.06	18.1	8.0	2.25	2.68	−0.42	/	0.694	/
CN-L@Pt	17.6	0.07	15.9	8.0	1.06	2.68	−1.68	1.19	0.626	0.652
CN-H	85.0	0.27	14.5	18.0	2.34	3.00	−0.73	/	0.627	/
CN-H@Pt	81.0	0.22	12.2	17.5	2.08	2.96	−0.95	0.26	0.402	0.431
TiO_2	93.3	0.53	19.6	25.0	2.89	3.26	−0.37	/	0.722	/
TiO_2@Pt	91.9	0.53	20.0	25.0	2.73	3.25	−0.52	0.16	0.246	0.270

[a] CB calculated from: CB = *Eg* − VB.
[b] SBH calculated from: $SBH = VB_{bare\ support} - VB_{bare\ support@Pt}$.
[c] Measured in the presence of BPA.

domains, indicating a higher degree of polymerization and greater textural development. After Pt deposition, the morphology of both carbon nitride supports is largely preserved. CN-L@Pt shows a slightly rougher and more granular surface compared to CN-L, while CN-H@Pt displays enhanced surface texture and compaction of the layered sheet-like carbon nitride structures. In both cases, the changes are subtle and consistent with the presence of finely dispersed Pt nanoparticles on the external surfaces of the carbon nitride aggregates. No large Pt

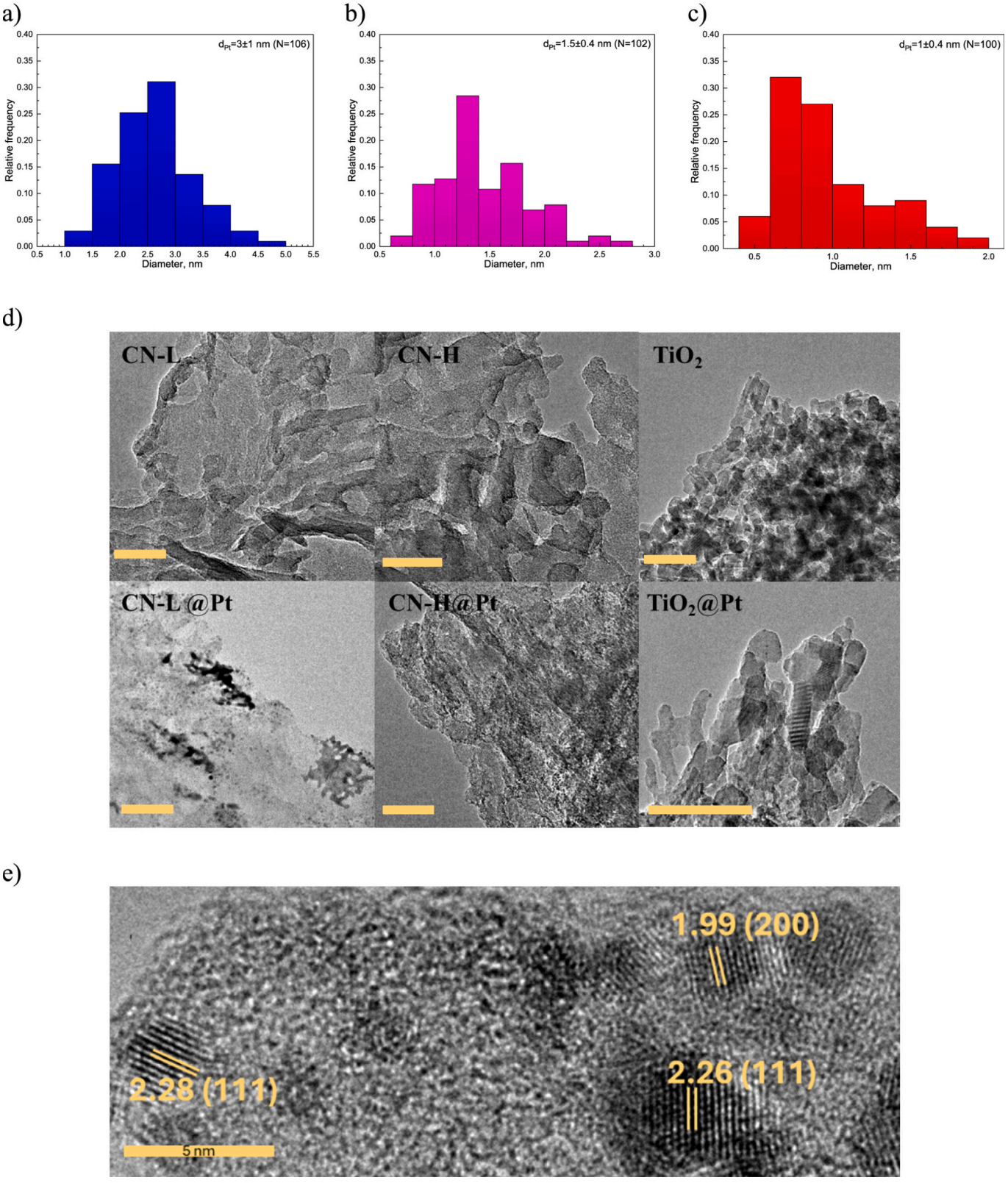

Fig. 2. Pt nanoparticle size distributions for a) CN-L@Pt, b) CN-H@Pt, and c) TiO_2@Pt samples. d) TEM images of bare supports and Pt-loaded catalysts (scale bar: 50 nm). e) HR-TEM micrograph showing Pt nanoparticles embedded in the g-C_3N_4 matrix with visible (111) and (200) lattice planes.

clusters are visible, confirming nanoscale integration of Pt without structural disruption of the g-C_3N_4 framework. A markedly different morphology is observed for the TiO_2 sample, which consists of uniform, high-aspect-ratio nanorods forming an open, interconnected network. This rod-like architecture is maintained after Pt deposition, with the nanorods remaining well defined and structurally intact. This is consistent with the unchanged BET surface area and the preserved anatase XRD pattern, confirming that Pt deposition does not alter the TiO_2 nanorod assembly.

SEM-EDX elemental analysis further confirms the successful incorporation of Pt into all Pt-modified catalysts (Fig. S5, Table S1). The pristine supports show only their expected elemental compositions, C and N for CN-L and CN-H, and Ti and O for TiO_2, while additional Pt signals are clearly detected in CN-L@Pt, CN-H@Pt, and TiO_2@Pt. Quantitative determination of Pt loading by ICP-OES shows Pt contents close to the nominal 1 wt% value for all Pt-modified samples (Table S1), demonstrating good control of the impregnation procedure. These values agree well with the semi-quantitative Pt contents obtained from SEM-EDX analysis, confirming the reliability of the measured metal loadings. SEM-EDX mapping images (Fig. S5) further show that Pt is homogeneously distributed across all support surfaces. Pt dispersion is particularly uniform in CN-H@Pt, reflecting the higher surface area and more accessible mesopores of CN-H, which promote more effective Pt anchoring. In CN-L@Pt, Pt remains well distributed but forms slightly larger domains, consistent with the lower surface area of CN-L and the more pronounced Pt reflections observed in its XRD pattern. On TiO2@Pt, Pt is evenly dispersed along the external facets of the nanorods, although the nanoparticles remain too small to be resolved in SEM.

These SEM observations correlate well with the TEM analysis (Fig. 2), which directly resolves the Pt NPs and confirms the differences in Pt dispersion inferred from SEM and XRD. The g-C_3N_4 samples show the expected layered, wrinkled texture in TEM, with CN-L forming dense aggregates of thicker layered domains, whereas CN-H consists of thinner, more open, layered sheet-like domains with reduced stacking thickness. TiO_2 again displays uniform anisotropic nanorods. Pt deposition preserves the structural features of all supports while introducing well-dispersed Pt nanoparticles on CN-H and TiO_2, and a combination of dispersed nanoparticles and larger aggregates on CN-L. Quantitative TEM analysis (excluding large aggregates for CN-L) reveals average Pt NPs sizes of 1.5 ± 0.4 nm for CN-H@Pt, 3 ± 1 nm for CN-L@Pt, and 1.0 ± 0.4 nm for TiO_2@Pt (Fig. 2), demonstrating the strong influence of support textural properties on Pt nucleation and growth. Importantly, these TEM findings are fully consistent with the XRD analyses. Clear Pt reflections appear only for CN-L@Pt, which contains larger Pt NPs (~3 nm), whereas CN-H@Pt and TiO_2@Pt show no detectable Pt diffraction peaks because their Pt particles (~1 to 1.5 nm) fall below the standard XRD detection threshold. This direct correlation confirms that the presence or absence of Pt signals in XRD is governed primarily by NPs size rather than by differences in loading. High-resolution TEM images further show lattice fringes corresponding to the (111) and (200) planes of metallic Pt, confirming the polycrystalline nature of the nanoparticles. STEM-EDXS mapping (Fig. S6) verifies homogeneous Pt distribution in CN-H@Pt and TiO_2@Pt, while CN-L@Pt displays a broader distribution consistent with partial aggregation. The combined SEM, TEM, and STEM-EDX results clearly show that the intrinsic textural properties of the supports, including surface area, layered sheet-like morphology, and porosity, play a decisive role in determining Pt nucleation, dispersion, and aggregation. These structural differences directly affect the electronic properties and charge-transfer behaviour discussed in the following sections.

Zeta potential measurements offer key insights into the surface charging behaviour of the investigated supports and, consequently, their interaction with the Pt precursor species during synthesis (Fig. S7). Both carbon nitride materials exhibit strongly pH-dependent behaviour typical of polymeric g-C_3N_4 [29]. CN-L shows moderately negative potentials across pH 2–7, while CN-H, due to its higher density of deprotonated nitrogen functionalities and more open nanostructure, displays substantially more negative values over the entire pH range. In contrast, TiO_2 exhibits the characteristic amphoteric profile of metal oxides, with positive potentials at acidic pH, a point of zero charge near pH value of 6.5, and only slightly negative values at pH ≥ 7 [34]. At the Pt deposition pH of 8, the differences between the supports are most pronounced. Both CN-L and especially CN-H exhibit strongly negative surface potentials (−20 to −35 mV), which promote efficient electrostatic adsorption of hydrolyzed Pt species and favour uniform precursor distribution across the surface. TiO_2, however, displays a near-neutral potential, indicating a considerably weaker Coulombic driving force for precursor anchoring. These electrostatic characteristics directly correlate with the Pt nanoparticle sizes and distributions observed by TEM for g-C_3N_4 supports. The highly negative potential of CN-H enables dense nucleation of Pt clusters, resulting in the smallest particles (1.5 nm). CN-L, with a less negative surface and more compact morphology, forms larger Pt nanoparticles (3 nm). Although TiO_2 lacks the strong electrostatic attraction observed for g-C_3N_4, its high surface area and abundance of surface hydroxyls still enable effective Pt anchoring, yielding uniformly dispersed, ultra-small Pt nanoparticles (1.0 nm). Together, these results demonstrate that surface charge is a primary factor governing Pt nucleation, but it acts in synergy with textural properties and surface chemistry. Strongly negative g-C_3N_4 surfaces favour electrostatic precursor binding and high nucleation density, whereas Pt deposition on TiO_2 proceeds predominantly via chemical interactions with surface hydroxyls. These correlations confirm that surface charge, in combination with textural features and surface chemistry, directly governs Pt nucleation and growth across the three supports, fully explaining the nanoparticle size distributions observed by TEM.

3.2. Surface chemistry and electronic structure of catalysts

The UV–Vis diffuse reflectance spectra of the photocatalysts studied are shown in Fig. S8a, and the corresponding Tauc plots, derived from the Kubelka-Munk function, are presented in Fig. S8b. Pristine TiO_2 exhibits a steep absorption edge at 380 nm, typical of anatase, with no absorption in the visible region [6]. The determined band-gap energy (*Eg*) is 3.26 eV (Table 1). After Pt deposition, the fundamental absorption edge of TiO_2@Pt remains essentially unchanged ($Eg(TiO_2@Pt) = 3.25$ eV), but a pronounced absorption tail extending deep into the visible region appears. This additional absorption arises from Pt-related interband and/or plasmonic transitions, indicating that Pt can act as a visible-light sensitizer on TiO2 [35]. In contrast, the g-C_3N_4 materials display intrinsic absorption well into the visible range. CN-L shows an absorption edge around 460 nm, corresponding to a band gap of 2.67 eV, whereas CN-H exhibits a slightly blue-shifted edge with $Eg = 3.07$ eV, consistent with its more condensed heptazine structure. Pt deposition slightly modifies the optical response of both carbon nitride samples. For CN-L@Pt, the band gap increases marginally to 2.74 eV, while CN-H@Pt shows a small decrease to 3.03 eV. In both cases, the overall absorbance in the visible region increases compared to the pristine supports, reflecting the additional contribution of Pt nanoparticles and possible changes in surface electronic states. These UV–Vis DRS results confirm that TiO_2 remains a wide-band-gap UV absorber, whereas g-C_3N_4 provides intrinsic visible-light activity, and that Pt loading mainly enhances sub-band-gap absorption without significantly altering the fundamental band gaps of the supports. The extracted *Eg* values will be combined with the valence-band positions obtained from XPS to construct the band alignment diagrams and to discuss Schottky barrier formation and charge-transfer pathways in the following section.

The XPS survey spectra of all investigated samples (Fig. S9) confirm the expected elemental composition of the photocatalysts. The pristine g-C_3N_4 materials (CN-L and CN-H) show only carbon (C 1s) and nitrogen (N 1s) signals, with no evidence of impurities within the detection limit of the instrument. After Pt deposition, an additional Pt 4f signal appears

in both CN-L@Pt and CN-H@Pt, confirming the successful incorporation of Pt into the carbon nitride structure without introducing foreign elements. The TiO_2 samples exhibit the characteristic Ti 2p and O 1s peaks of anatase TiO_2, while TiO_2@Pt also shows a clear Pt 4f contribution. As expected, no nitrogen is detected in either TiO_2 sample. The C 1s peak at 284.8 eV present in all spectra originates from adventitious carbon and is used for charge calibration. Overall, the survey spectra demonstrate that all photocatalysts are chemically pure and that Pt deposition proceeds efficiently on all supports.

The Ti 2p high-resolution spectra of TiO_2 and TiO_2@Pt (Fig. 3) display the characteristic spin-orbit doublet of Ti^{4+} in anatase TiO_2 [36,37]. For pristine TiO_2, the Ti $2p_{3/2}$ and Ti $2p_{1/2}$ peaks are located at 458.7 eV and 464.4 eV, respectively. Upon Pt deposition, both peaks shift slightly to 458.9 eV and 464.6 eV, changes well within typical experimental variation. These small positive shifts indicate weak electron redistribution at the Pt/TiO_2 interface and are consistent with the formation of a Schottky junction, but do not reflect any change in Ti oxidation state. Importantly, no Ti^{3+} features are observed, confirming that TiO_2 remains fully oxidized and structurally intact after Pt loading and reduction process. This is consistent with the preserved BET surface area and XRD pattern of TiO_2@Pt.

The C 1s spectra of the g-C_3N_4 materials (Fig. 3) show two characteristic components. A dominant peak at 288.2 eV corresponds to sp^2-hybridized carbon in the N–C=N environment of heptazine units, confirming the structural integrity of g-C_3N_4 [28]. A second peak at 284.8 eV is attributed to adventitious carbon. In contrast, TiO_2 and TiO_2@Pt show only the 284.8 eV peak, confirming that no carbon-containing species are present on the TiO_2 surface and that Pt deposition does not introduce additional carbon functionalities.

The N 1 s spectra of CN-L, CN-H and their Pt-loaded analogues (Fig. 3) exhibit the typical features of heptazine-based carbon nitride. The main peak at 398.7 eV corresponds to sp^2 nitrogen in the C–N=C configuration, while the peak at 401.2 eV is assigned to bridging tertiary nitrogen (N–$(C)_3$) linking the heptazine units [28,38]. The peak shapes and relative intensities remain essentially unchanged after Pt deposition, indicating that the chemical environment of nitrogen is preserved and that the g-C_3N_4 framework remains intact.

The Pt 4f spectra (Fig. 3) provide insight into the oxidation state and electronic environment of Pt on the different supports. All Pt-containing samples display the characteristic Pt 4f spin-orbit doublet in the 70–77 eV region. Peak deconvolution (Fig. S10) reveals a clear support-dependent distribution of Pt oxidation states (Table S1). On the carbon nitride supports, both CN-L@Pt and CN-H@Pt exhibit a mixed Pt^0/Pt^{2+} character. In CN-L@Pt, the Pt $4f_{7/2}$ component at 71.3 eV and the Pt^{2+} contribution at 72.8 eV correspond to approximately 70% Pt^0 and 30% Pt^{2+}, while CN-H@Pt shows an increased Pt^{2+} fraction of about 40% [37]. This stabilization of oxidized Pt species is characteristic of Pt supported on nitrogen-rich materials and reflects strong metal-support interactions involving Pt—N coordination and partial charge transfer from Pt to the carbon nitride framework. In contrast, TiO_2@Pt contains only metallic Pt^0, indicating more complete reduction of Pt species and a fundamentally different electronic interaction between Pt and the oxide surface. This distinct Pt electronic structure on TiO_2 is consistent with stronger electronic coupling and efficient Fermi-level equilibration between Pt and the TiO_2 conduction band. These results show that Pt does not exhibit identical chemical behaviour across the different supports, despite identical nominal synthesis conditions. Instead, the observed differences in Pt oxidation state are intrinsic consequences of support-dependent metal-support interactions. These differences in Pt electronic structure correlate directly with the contrasting charge-transfer dynamics, ROS selectivity, and photocatalytic performance observed for TiO_2- and g-C_3N_4-based catalysts. The Pt^{2+} components observed in g-C_3N_4-supported samples do not originate from residual precursor species, as indicated by the absence of chlorine in the XPS survey spectra

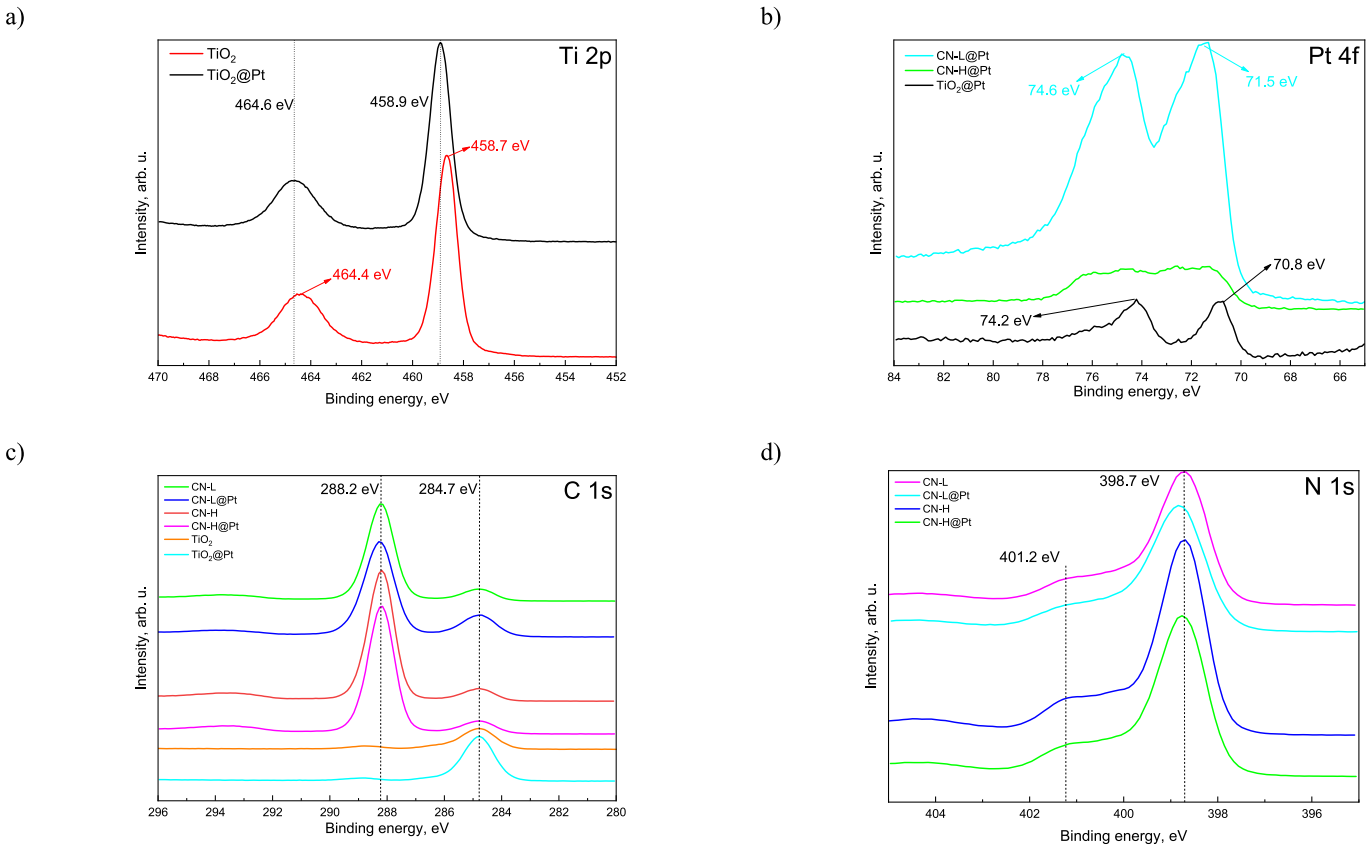

Fig. 3. XPS high-resolution spectra for a) Ti 2p, b) Pt 4f, c) C 1s, and d) N 1s of the examined materials.

and the complete lack of Pt^{2+} contributions in TiO_2@Pt prepared under identical conditions. Instead, they reflect Pt atoms stabilized at the Pt—N interface.

The valence band regions of the XPS spectra were recorded for all photocatalysts, and the valence band maxima (VBM) were determined by linear extrapolation of the leading edge to the baseline (Fig. S9b–d). The obtained VBM values were combined with the optical band gaps derived from UV–Vis DRS (Table 1) to construct the band-edge diagram (Fig. S9e) and to estimate the effective Schottky barrier heights (SBH) at the Pt/semiconductor interfaces (Table 1). For the pristine g-C_3N_4 samples, the VBM values of 2.25 eV for CN-L and 2.34 eV for CN-H are in good agreement with literature reports for polymeric carbon nitride [39]. Using the corresponding optical band gaps (2.67 eV for CN-L and 3.07 eV for CN-H, Table 1), the conduction band (CB) positions are estimated at −0.42 eV and −0.73 eV, respectively. These CB levels are sufficiently negative to thermodynamically enable O_2 reduction to superoxide anion radicals, while the VB positions lie close to the threshold required for hydroxyl radical formation [40,41]. Pt deposition induces pronounced changes in the apparent band alignment of the g-C_3N_4 materials, particularly for CN-L. In CN-L@Pt, the VBM shifts to lower binding energy (1.06 eV), and, together with the slightly widened band gap (2.74 eV), this corresponds to an apparent upshift of the CB to −1.68 eV. The estimated apparent effective Schottky barrier height (SBH), derived from XPS valence band extrapolation at the Pt/CN-L interface, is 1.19 eV. This large apparent barrier indicates pronounced interfacial band bending and a substantial thermodynamic driving force for electron transfer from g-C_3N_4 to Pt under equilibrium conditions. As a consequence, hole-driven hydroxyl radical formation is expected to be

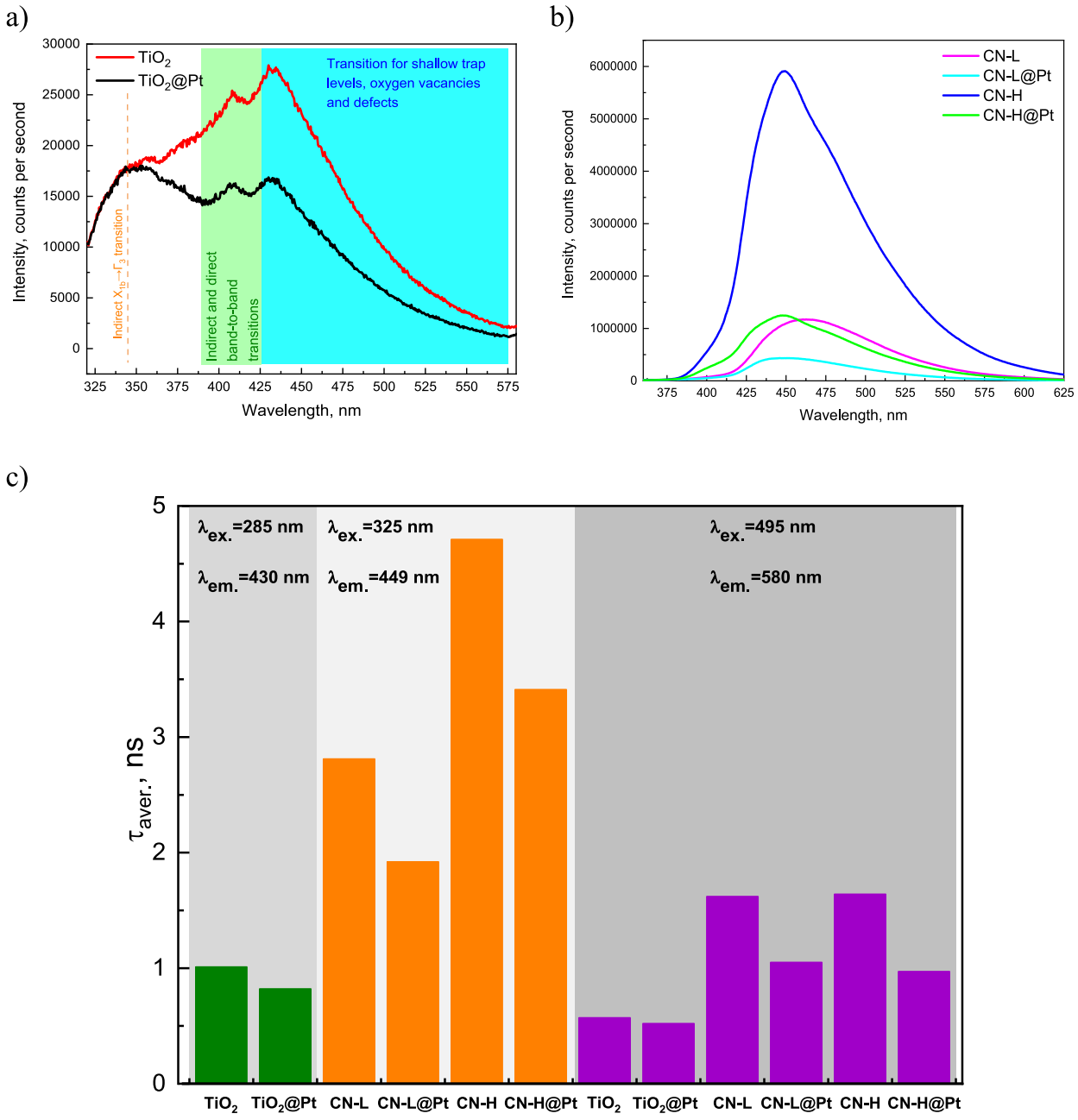

Fig. 4. a) Solid state PL spectra of bare TiO_2 and TiO_2@Pt (excitation wavelength: 300 nm; scan performed in 0.5 nm steps with an integration time of 0.5 s; slit width: 8 nm). b) Solid state PL spectra of bare and Pt-modified g-C_3N_4 (CN-L, CN-H, CN-L@Pt, CN-H@Pt) (excitation wavelength: 325 nm; scan performed in 0.5 nm steps with an integration time of 0.5 s; slit width: 8.9 nm). c) Average lifetimes obtained from TCSPC measurements under different excitation-emission conditions, illustrating the impact of Pt deposition on the photocarrier decay dynamics of the investigated materials.

strongly suppressed, consistent with the reduced $OH^{\bullet}$ generation observed experimentally [40,41]. In CN-H@Pt, the band-edge modifications are more moderate. The VBM shifts slightly to 2.08 eV, the optical band gap becomes 3.03 eV, and the CB is located at approximately −0.95 eV. The corresponding effective SBH of 0.26 eV indicates weaker band bending than in CN-L@Pt, while still favouring electron extraction to Pt. Importantly, the VB position of CN-H@Pt remains close to the $OH^{\bullet}$ formation threshold, which is consistent with its comparatively higher oxidative capability relative to CN-L@Pt. Pristine TiO_2 exhibits a VBM at 2.89 eV and a band gap of 3.26 eV, placing the CB at −0.37 eV. This highly positive VB position explains the strong oxidizing power of TiO_2 holes. After Pt deposition, the VBM of TiO_2@Pt shifts slightly to 2.73 eV, while the band gap remains essentially unchanged (3.25 eV), resulting in a CB position of −0.52 eV. The estimated effective SBH at the Pt/TiO_2 interface is 0.16 eV, indicating modest band bending that is nevertheless sufficient for efficient electron trapping on Pt without substantially compromising the oxidizing strength of the VB. Overall, the combined UV–Vis DRS and valence-band XPS analysis reveals a pronounced support-dependent influence of Pt deposition on band alignment and interfacial energetics. On TiO_2, Pt induces only minor shifts of the band edges and forms a low effective Schottky barrier, preserving the strong oxidative potential of the VB and enabling efficient Pt-mediated ROS formation. On g-C_3N_4, particularly CN-L, Pt induces much stronger apparent band bending, favouring superoxide-based reduction pathways at the expense of hydroxyl radical formation. These support-dependent electronic effects provide a consistent framework for understanding the distinct ROS profiles and photocatalytic behaviours of TiO_2@Pt and CN@Pt discussed in the following sections.

3.3. Optoelectronic properties and excited-state dynamics of catalysts

The PL spectra of the photocatalysts (Fig. 4) provide insight into the radiative recombination pathways of photogenerated charge carriers, including band-to-band transitions and defect-mediated emission. As is typical for wide-band-gap oxides, pristine TiO_2 exhibits a broad emission band between 370 and 550 nm. This emission originates from the recombination of electrons in shallow or deep defect states, primarily oxygen vacancies and Ti^{3+}-related centers, with holes in the valence band [42]. After Pt loading, the overall PL intensity decreases significantly across the entire spectral range. This pronounced quenching reflects efficient extraction of photogenerated electrons from the TiO_2 conduction band into the Pt nanoparticles, which act as electron sinks and suppress radiative recombination. Such PL attenuation is consistent with the presence of a Pt/TiO_2 Schottky junction, as confirmed by the XPS band alignment analysis, and demonstrates enhanced charge separation in TiO_2@Pt [15,16]. The g-C_3N_4-based photocatalysts display different PL behaviour that reflects the molecular electronic structure of polymeric carbon nitride [22,29]. All CN samples exhibit a characteristic broad emission centered at 430–480 nm, which arises from intrinsic π-π* recombination within the heptazine framework, combined with defect-related emissive states associated with residual amino groups, surface vacancies, and incomplete polymerization. Among the pristine carbon nitrides, CN-H shows the strongest PL intensity, consistent with its more extensively condensed structure, which stabilizes radiative π-π* transitions. In contrast, CN-L exhibits substantially weaker PL emission, typical of less polymerized carbon nitride with a higher density of non-radiative pathways and localized defect states. Pt deposition leads to strong quenching of PL emission in both CN-L and CN-H. For CN-L@Pt, the PL intensity decreases by more than one order of magnitude, while CN-H@Pt exhibits even more pronounced suppression. This PL quenching arises from rapid ultrafast transfer of electrons from the g-C_3N_4 conduction band into Pt nanoparticles, providing a non-radiative recombination channel that efficiently competes with the intrinsic emissive transitions of g-C_3N_4. The extent of quenching mirrors the electronic structure derived from XPS. Although CN-L has a more negative conduction band minimum (−1.68 eV) than CN-H (−0.95 eV), this thermodynamic driving force alone does not determine the efficiency of interfacial electron transfer. In defect-rich polymeric carbon nitrides, kinetic factors such as carrier lifetime, trap-state density, and interfacial electronic coupling govern the fraction of electrons that can be effectively extracted. This accounts for the superior charge-transfer behaviour observed for CN-H@Pt, despite its less negative conduction band position. Meanwhile, the lower PL intensity of pristine CN-L compared to CN-H also reflects its higher concentration of defect-assisted non-radiative pathways. To further clarify the origin of these emissive processes, the PL spectra of CN-L, CN-H, and their Pt-loaded counterparts were deconvoluted using a three-peak Gaussian model (Fig. S11, Table S2). The deconvoluted profiles reveal three characteristic contributions: (i) a π-π transition associated with intrinsic band-to-band recombination, (ii) a defect-related emission originating from nitrogen vacancies and residual –NH_x groups, and (iii) a deeper trap-state component linked to surface-localized defects [22,29]. Pristine CN-H exhibits a larger π-π contribution and a lower proportion of deep-trap emission compared to CN-L, consistent with its higher structural condensation and reduced defect density. Upon Pt deposition, all three emissive bands are strongly suppressed, with the most pronounced quenching in the defect- and trap-state components. This trend demonstrates that Pt nanoparticles preferentially extract electrons from defect-derived states, the dominant recombination channels in g-C_3N_4, thereby depleting both shallow and deep radiative pathways. The selective quenching observed in the deconvolution analysis is fully consistent with the TCSPC results (discussed below), which show accelerated decay of long-lived emissive populations, and confirms that Pt efficiently suppresses defect-mediated recombination in carbon nitride. While these optical signatures clearly indicate efficient interfacial charge extraction upon Pt deposition, direct experimental visualisation of band bending or interfacial electric fields at the Pt/g-C_3N_4 interface is beyond the scope of this study. Therefore, the formation of a Schottky-type metal-semiconductor contact in the CN-based systems is inferred from consistent indirect experimental evidence, including pronounced PL quenching, lifetime shortening, and enhanced photoelectrochemical charge transfer, rather than from direct measurements. Notably, recent *operando* and in situ spectroscopic studies have directly demonstrated Fermi-level equilibration, interfacial electric field formation, and band bending at noble metal/semiconductor interfaces, thus providing strong physical validation for the Schottky-driven charge separation mechanism invoked here [43]. Overall, the PL analysis confirms that Pt NPs effectively suppress radiative electron-hole recombination for all there supports. The combination of steady-state quenching, PL deconvolution, and lifetime shortening provides a coherent picture in which Pt NPs selectively extracts photoexcited electrons from both intrinsic and defect-derived emissive states, thus enhancing charge separation and prolonging carrier lifetimes, consistent with the electronic band alignment and Schottky barriers determined from XPS.

To gain deeper insight into the carrier relaxation pathways, TCSPC measurements were performed under three different excitation-emission conditions, each designed to selectively probe a specific emissive channel: (1) excitation at 285 nm and emission at 430 nm to excite only TiO_2 (Fig. S12a, d), (2) excitation at 325 nm and emission at 449 nm to excite only g-C_3N_4 (Fig. S12b, e), and (3) excitation at 495 nm and emission at 580 nm to excite only Pt-related states (Fig. S12c,f). All decay curves were fitted bi-exponentially, and the amplitude-weighted lifetime ($\tau_{aver.}$) was used for comparison. χ^2 values close to unity indicate good quality fit (Table S3).

When TiO_2 is excited at 285 nm and emission is monitored at 430 nm, the decay of pristine TiO_2 is dominated by a fast component of 0.66 ns ($A_1 = 90.6\%$) and a minor slower component of 4.39 ns ($A_2 = 9.4\%$), giving an average lifetime of $\tau_{aver.} = 1.01$ ns. These components are attributed to rapid recombination via shallow defect states and a small fraction of longer-lived trapped carriers, respectively [44]. After Pt deposition, the decay profile of TiO_2@Pt is strongly modified. The

predominant component is now 0.59 ns ($A_2 = 93.3\%$) with only a minor contribution from a longer-lived channel (3.96 ns, $A_1 = 6.7\%$), resulting in a slightly shorter average lifetime of 0.82 ns. The disappearance of most of the long-lived emissive population and the overall acceleration of the decay are consistent with efficient electron transfer from TiO_2 to Pt, which introduces a fast non-radiative channel and suppresses defect-mediated radiative recombination [45]. These TCSPC trends fully agree with the steady-state PL quenching observed for TiO_2@Pt. Under excitation at 325 nm and detection at 449 nm, the decays probe predominantly the intrinsic emission of g-C_3N_4. For CN-L, the decay consists of a short component of 1.85 ns ($A_2 = 88.6\%$) and a minor slower one of 10.15 ns ($A_1 = 11.4\%$), giving $\tau_{aver.} = 2.80$ ns. Pt deposition shortens both components (to 0.13 ns and 7.58 ns for CN-L@Pt) and reduces the average lifetime to 0.88 ns, indicating the introduction of an additional ultrafast non-radiative pathway associated with electron transfer to Pt. The difference is even more pronounced for CN-H. Pristine CN-H displays much longer lifetimes, with $\tau_1 = 28.3$ ns ($A_1 = 86.6\%$) and $\tau_2 = 16.9$ ns ($A_2 = 13.4\%$), corresponding to $\tau_{aver.} = 26.77$ ns, reflecting a substantial population of long-lived emissive states in the more condensed g-C_3N_4 framework. In CN-H@Pt, however, the dominant component collapses to 1.9 ns ($A_1 = 85.5\%$) with a secondary contribution at 12.1 ns ($A_2 = 14.5\%$), and the average lifetime decreases to 3.38 ns. The pronounced reduction of the long-lived component demonstrates that Pt nanoparticles efficiently extract electrons from CN-H, in line with the strong PL quenching and the favourable band alignment (CB at −0.95 eV) determined from XPS and UV–Vis DRS measurements. The contrasting behaviour of CN-L and CN-H can be directly attributed to their distinct structural and electronic characteristics. CN-L, being less condensed and containing a higher density of defect sites and terminal -NH_x functionalities, exhibits intrinsically weaker photoluminescence and shorter lifetimes because non-radiative pathways dominate its relaxation. In contrast, CN-H displays much stronger photoluminescence emission and significantly longer τ_1/τ_2 components, consistent with its more polymerized heptazine network and lower defect density, which stabilize long-lived emissive states. Consequently, Pt loading causes a more pronounced lifetime reduction in CN-H than in CN-L, highlighting stronger electronic coupling and more efficient interfacial charge extraction in the highly condensed CN-H structure. These differences in ultrafast dynamics are reflected in the UV–Vis and XPS band-edge analysis, demonstrating that the intrinsic electronic structure of g-C_3N_4 determines how effectively Pt can function as an electron sink. Additional TCSPC measurements were carried out using 495 nm excitation and 580 nm emission to probe the dynamics of Pt-related and low-energy defect states (Fig. S13). Under these conditions, all samples exhibit very fast decays dominated by sub-nanosecond components (Table S3). The average lifetimes are 0.58 ns and 0.51 ns for TiO_2 and TiO_2@Pt, respectively, and 1.61/1.06 ns for CN-L/CN-L@Pt and 1.65/0.98 ns for CN-H/CN-H@Pt. This behaviour is expected because TiO_2 does not absorb light at 495 nm. Therefore, the detected emission originates exclusively from Pt-related transitions. Pt exhibits intrinsically ultrafast relaxation due to its metallic electronic structure, and when Pt is interfaced with TiO_2, an additional rapid non-radiative channel becomes available through interfacial electron transfer from Pt into the TiO_2 CB. This extra decay pathway further accelerates relaxation, resulting in the shorter $\tau_{aver.}$ observed for TiO_2@Pt.

The slight shortening of $\tau_{aver.}$ upon Pt loading in the CN-based materials suggests efficient relaxation of photoexcited Pt or charge-transfer states via interfacial electron injection into the semiconductor, again consistent with the role of Pt as an electron sink and sensitizer under visible-light excitation. In summary, the TCSPC data reveal that Pt deposition systematically accelerates the decay of photoexcited states associated with both TiO_2 and g-C_3N_4, reflected in the strong suppression of long-lived emissive components and the reduction of the average PL lifetimes. Rather than indicating increased recombination, these shorter lifetimes at the monitored emission wavelengths signify the opening of rapid non-radiative charge-transfer channels towards Pt. Together with the steady-state PL quenching and the XPS-derived band alignment, the TCSPC results provide compelling evidence that Pt nanoparticles act as efficient electron traps, enhancing charge separation and underpinning the improved photocatalytic performance of the Pt-modified photocatalysts. Similar lifetime shortening and charge-transfer acceleration at metal-semiconductor interfaces have recently been elucidated in detail using advanced time-resolved and *operando* spectroscopic techniques. Notably, the mechanistic interpretation derived from the TCSPC results in this work is fully consistent with recent state-of-the-art studies on noble metal-modified photocatalysts [46]. At this stage, it is important to clarify the origin of visible-light-induced charge carriers in the investigated systems. For g-C_3N_4-based photocatalysts, visible-light excitation arises intrinsically from the polymeric carbon nitride framework, which directly absorbs visible photons and generates electron-hole pairs that are subsequently separated by Pt nanoparticles acting as electron sinks. In contrast, TiO_2 does not absorb visible-light under the applied irradiation conditions, as confirmed by UV–Vis diffuse reflectance spectroscopy. Accordingly, visible-light activity in TiO_2@Pt is predominantly governed by Pt-mediated excitation and interfacial charge-transfer processes, while possible sub-band-gap or defect-related contributions from TiO_2 remain secondary under the applied conditions. Given the ultrasmall size of the Pt nanoparticles, classical plasmonic hot-electron mechanisms are expected to be strongly damped. In this context, the spectroscopic and photoelectrochemical signatures primarily reflect efficient interfacial charge extraction and utilization rather than a single dominant excitation mechanism.

Solid-state EPR spectroscopy was used to identify paramagnetic centers in the investigated photocatalysts under dark conditions and visible-light irradiation (Fig. 5). All samples exhibit signals in the $g \approx 2.00$ region, but their intensity and response to illumination differ markedly between TiO_2- and g-C_3N_4-based materials, reflecting their fundamentally different defect structures and charge-trapping mechanisms. Pristine TiO_2 shows a composite EPR signal consisting of two nearly equally intense components. The first resonance at $g \approx 2.000$ originates from oxygen-centered trapped electrons ($O_2^{\bullet-}$ or O^- species at surface oxygen sites), while the second at $g \approx 1.996$ corresponds to Ti^{3+} shallow traps arising from electrons localized in Ti 3d orbitals [47]. Additional TiO_2-specific features are observed at $g \approx 1.979$ and $g \approx 1.948$, representing progressively deeper electron traps. The signal at $g \approx 1.979$ is assigned to surface Ti^{3+} centers in slightly distorted octahedral sites, while the feature at $g \approx 1.948$ corresponds to more strongly localized subsurface Ti^{3+}-oxygen-vacancy complexes (F-center-like states) [48,49]. A further low-field component at $g \approx 1.923$ is detected, indicating the deepest and most strongly bound trapped electrons in anatase, typically associated with bulk Ti^{3+} centers or highly localized Ti^{3+}–V^0–Ti^{4+} complexes [50]. Pt deposition slightly increases the overall signal intensity, suggesting a modest rise in the population of trapped electrons or stabilized defect centers. However, neither TiO_2 nor TiO_2@Pt shows any measurable increase in EPR intensity under visible-light irradiation (Fig. S14), demonstrating that anatase TiO_2 does not form additional paramagnetic centers when excited with visible-light. This observation is consistent with its minimal visible-light absorption shown in UV–Vis spectra. The presence of Ti^{3+} in EPR but not in Ti 2p XPS spectra is well documented for TiO_2 systems and reflects the far greater sensitivity of EPR to trace paramagnetic species, as well as the susceptibility of surface Ti^{3+} to re-oxidation during XPS analysis [51].

In contrast, all g-C_3N_4-based samples display a single, symmetric EPR line centered at $g \approx 1.999$, characteristic of π-radicals delocalized within the heptazine network [52]. In the dark, CN-L exhibits a more intense signal than CN-H, consistent with its higher density of intrinsic defects, terminal –NH_x groups, and unsaturated edge sites capable of stabilizing unpaired electrons. Upon visible-light irradiation, both CN-L and CN-H show a clear and significant increase in EPR intensity (Fig. S14), demonstrating that carbon nitride efficiently absorbs visible-light and forms additional photoinduced π-radicals or trapped electrons that are

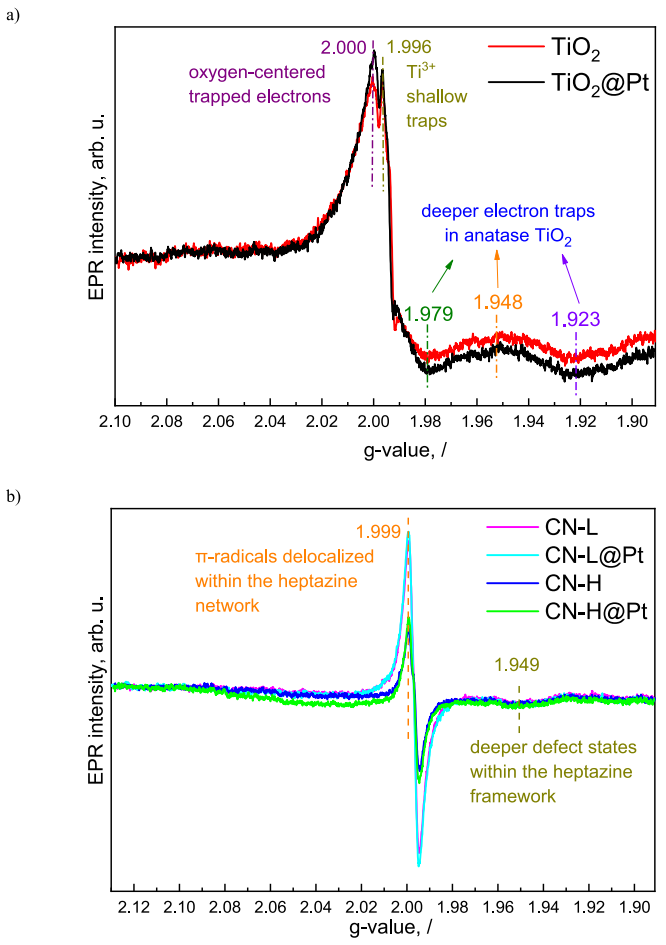

Fig. 5. EPR spectra of the synthesized a) TiO_2 and b) CN-based materials. The spectra were recorded in the X-band under dark ambient conditions using a modulation amplitude of 450 μT, a power attenuation of 18 dB and a gain of 1 × 10^3.

sufficiently long-lived to be detected by EPR. For the Pt-modified carbon nitride samples, Pt deposition leads to a higher baseline EPR signal intensity and promotes the stabilization of photoinduced paramagnetic centers, consistent with enhanced charge separation inferred from PL, TCSPC, and EIS measurements. In addition to the dominant π-radical signature, the CN samples also display a weaker low-field shoulder at g ≈ 1.949. This feature is characteristic of strongly localized nitrogen-centered radicals or electrons trapped at nitrogen vacancies, representing deeper defect states within the heptazine framework [53]. Such low-g components have previously been reported for defect-rich g-C_3N_4 and reflect highly localized, low-symmetry trap sites, distinct from the delocalized π-radicals. Pt deposition amplifies this behaviour further. Both CN-L@Pt and CN-H@Pt exhibit a stronger light-induced increase in EPR signal intensity compared to their pristine counterparts, indicating that Pt promotes charge separation by efficiently extracting photogenerated electrons from the CN framework and stabilizing them in nearby π-radical centers. Although the structural differences between CN-L and CN-H influence their intrinsic defect density, both Pt-modified samples show a very similar light-induced increase in EPR intensity, indicating that Pt strongly enhances charge separation in carbon nitride in both cases. This behaviour is fully consistent with steady-state PL quenching, TCSPC lifetime shortening, and XPS derived band alignment, all of which demonstrate efficient Pt assisted charge separation in both CN systems. Overall, the EPR results reveal a clear dichotomy in visible-light response. TiO_2-based materials show no detectable formation of additional paramagnetic centers under visible-light irradiation, whereas all g-C_3N_4-based samples exhibit a pronounced increase in radical population upon illumination. Pt selectively enhances this effect in carbon nitride by promoting electron extraction and stabilization, while its influence on TiO_2 remains limited under visible-light. These findings provide direct spectroscopic evidence that g-C_3N_4 is the primary visible-light absorber in the studied systems and that Pt plays a critical role in improving charge separation and radical formation in the CN materials, thereby contributing to their superior photocatalytic performance.

The photoelectrochemical characterization, comprising transient photocurrent measurements and electrochemical impedance spectroscopy (EIS), provides a direct assessment of charge-carrier separation efficiency and interfacial charge-transfer kinetics in the synthesized photocatalysts. All measurements were performed under visible-light irradiation, ensuring that the observed responses originate exclusively from sub-band-gap or Pt-assisted excitation pathways. All Pt-modified samples exhibit significantly enhanced photocurrent responses compared to their pristine counterparts (Fig. S15a), confirming the role of Pt as an efficient electron sink that facilitates rapid extraction of photogenerated electrons and suppresses electron-hole recombination. Among the CN-based materials, CN-H@Pt generates the highest steady-state photocurrent, consistent with its superior Pt dispersion, higher surface area, and more favourable electronic structure, as established by TEM and XPS analyses. In contrast, CN-L@Pt displays only a moderate increase relative to CN-L, reflecting less efficient charge separation arising from larger Pt particles and the more defect-rich CN-L framework. EIS Nyquist plots (Fig. S15b) further substantiate these trends. Fitting with the equivalent circuit (Fig. S15c) yields markedly lower charge-transfer resistance (R_{CT}, Table 1) values for all Pt-containing samples, indicating accelerated interfacial electron transfer at the semiconductor-electrolyte interface. As the EIS measurements were also conducted under visible-light illumination, the reduced semicircle diameters directly reflect the improved charge-transfer kinetics enabled by Pt-mediated visible-light activation. TiO_2@Pt exhibits the lowest R_{CT} (0.246 MΩ), followed by CN-H@Pt (0.402 MΩ) and CN-L@Pt (0.626 MΩ), mirroring the photocurrent behaviour and the trend observed in Pt nanoparticle sizes. Notably, the R_{CT} values of the pristine supports are substantially higher (0.627–0.722 MΩ), underscoring the decisive influence of Pt in lowering the Schottky barrier height (SBH) and enabling faster electron extraction. These electrochemical results are fully consistent with TEM-derived Pt particle sizes and surface charge properties. CN-H@Pt, which possesses the smallest Pt nanoparticles (1.5 nm) and the most negative zeta potential at the deposition pH, exhibits the most effective charge separation among the g-C_3N_4 samples. Conversely, CN-L@Pt, characterized by larger Pt domains (3 nm) and a less negative surface potential, shows weaker improvement, demonstrating how nucleation density and support surface chemistry govern interfacial catalytic kinetics. TiO_2@Pt, featuring the smallest Pt NPs overall (1.0 nm) and the lowest SBH (0.16 eV), displays the highest charge-transfer efficiency, particularly under visible-light excitation, consistent with the strong electronic coupling between Pt and the anatase conduction band. To further assess the impact of pollutant adsorption on interfacial charge-transfer properties, additional EIS measurements were performed in the presence of 10 mM BPA under otherwise identical experimental conditions (Fig. S15d, Table 1). Although the absolute R_{CT} values increase with BPA due to surface adsorption and reaction intermediates, the relative trend among the photocatalysts remains unchanged. This confirms that the observed support-dependent differences in interfacial charge-transfer efficiency are intrinsic to the catalyst systems and not an artefact of pollutant adsorption. Overall, the photocurrent and EIS analyses reveal a coherent structure-property-function relationship, where smaller Pt NPs and lower SBH values systematically enhance photocarrier separation and interfacial charge-transfer efficiency, even under visible-light illumination where intrinsic semiconductor excitation is limited. This behaviour is in excellent agreement with the optical (PL/TCSPC), structural (TEM, XRD), and surface electronic (XPS, zeta potential) characterization data.

It should be noted that, while the combined PL, TCSPC, EPR, and photoelectrochemical results clearly confine visible-light activity in the investigated systems to Pt-related states, the microscopic origin of this excitation cannot be unambiguously assigned to a single mechanism. Possible contributions include intraband excitation of Pt NPs, ligand-to-metal charge-transfer processes involving surface adsorbates, and photothermal effects. Importantly, regardless of the exact excitation pathway, all observable visible-light-induced reactivity in TiO_2@Pt originates from Pt rather than the TiO_2 lattice; while in g-C_3N_4-based systems, Pt primarily acts as an electron-extraction and charge-separation promoter.

3.4. Photodegradation of BPA and mechanistic analysis of reactive oxygen species

The visible-light degradation of water-dissolved bisphenol A (BPA) reveals fundamental mechanistic differences between Pt-modified TiO_2 and g-C_3N_4 photocatalysts, arising directly from their contrasting optical

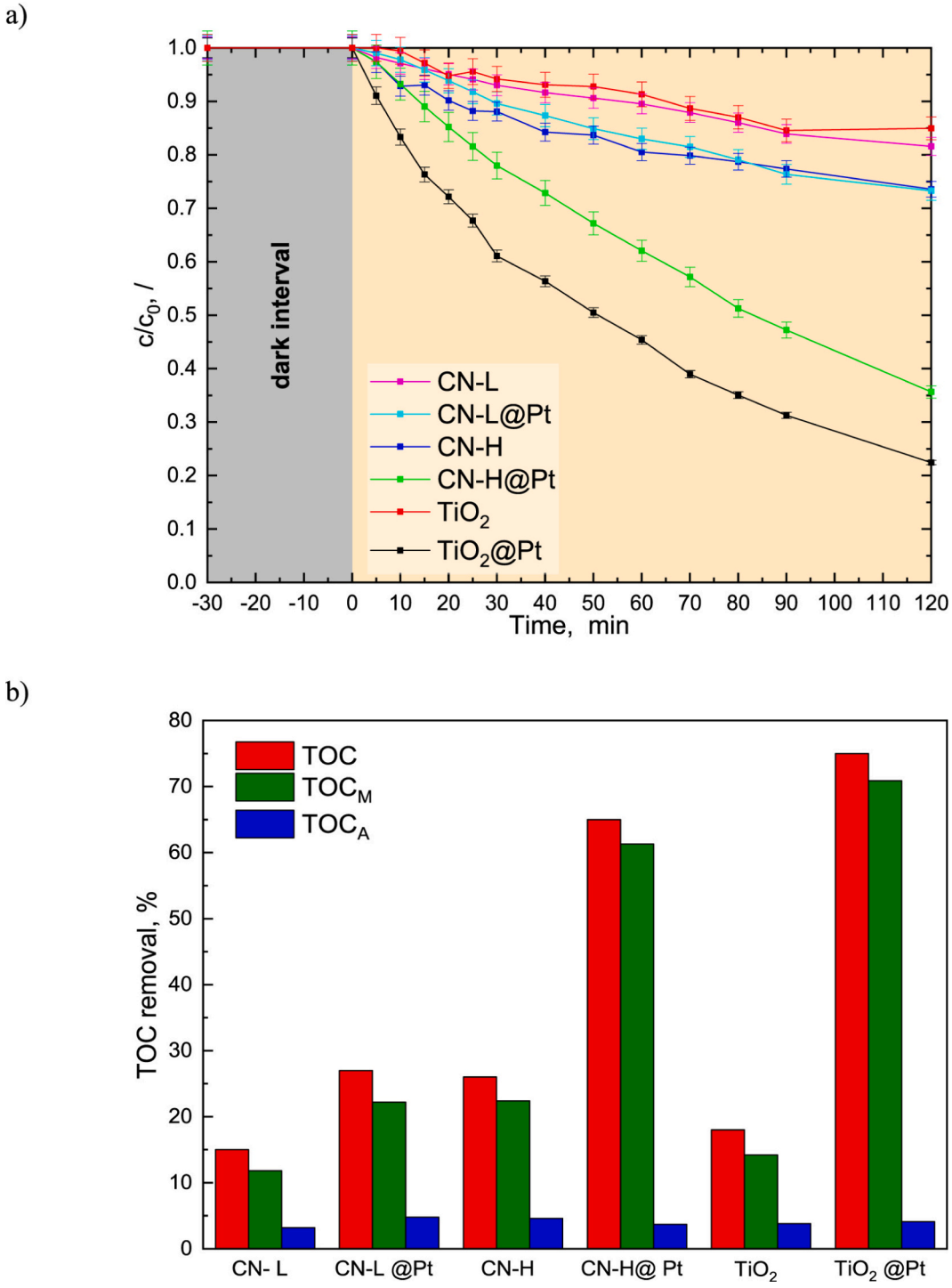

Fig. 6. a) Photocatalytic degradation of bisphenol A (BPA) in aqueous solution under visible-light irradiation using the photocatalysts studied. Error bars represent ± standard deviation from three independent experiments. b) Total organic carbon (TOC) analysis after the BPA degradation tests, showing overall TOC removal and its contributions from mineralized carbon (TOC_M) and accumulated intermediate species (TOC_A).

and electronic properties (Fig. 6a). To distinguish the intrinsic semiconductor photoresponse from cocatalyst-induced effects, all optoelectronic and photocatalytic properties were evaluated by comparing pristine and Pt-modified variants of the same support under visible-light irradiation ($\lambda > 410$ nm), rather than by cross-comparison between TiO_2 and g-C_3N_4 as direct photocatalytic systems. Importantly, the support-dependent contrast persists even when comparing Pt-modified samples with comparable surface area (CN-H@Pt and TiO_2@Pt), confirming that the observed mechanistic differences cannot be attributed solely to the intrinsic photoabsorption properties of the semiconductors, but instead arise from fundamentally different interfacial electronic interactions with Pt nanoparticles. As anatase TiO_2 does not absorb visible-light, it cannot generate electron-hole pairs under the illumination conditions used here (Fig. S1), and electron transfer from TiO_2 to Pt is therefore not possible. It should be noted that, although anatase TiO_2 does not undergo intrinsic band-to-band excitation under visible-light irradiation, weak but measurable photoresponses may still arise from sub-band-gap defect states, band-tail states, or surface-assisted charge-transfer processes involving adsorbed species. These contributions can account for the small photocurrent observed for pristine TiO_2 (Fig. S15a) and the limited photoactivity detected under visible-light conditions, but they remain fundamentally distinct from true semiconductor photogeneration and are several orders of magnitude weaker than the responses observed for Pt-modified systems. Consequently, the strong BPA degradation observed for TiO_2@Pt originates exclusively from Pt-centered visible-light excitation pathways, including ligand-to-metal charge-transfer transitions involving surface hydroxyls and water, and Pt-assisted oxygen activation through redox cycling between Pt^0 and Pt^{2+}. Notably, TiO_2@Pt shows substantial visible-light photocatalytic activity despite the negligible intrinsic absorption of TiO_2 above 410 nm. This further confirms that the enhanced reactivity under visible-light irradiation does not originate from bulk semiconductor excitation, but from Pt-mediated interfacial processes that dominate the photoresponse under the applied conditions. These processes are consistent with the pronounced PL quenching, the absence of long-lived luminescence components in TCSPC, and the weak EPR response of TiO_2 under visible-light, all of which confirm that TiO_2 remains optically inactive and serves only as a high-surface-area scaffold for Pt. The exceptionally low charge-transfer resistance and small Schottky barrier height (0.16 eV) further explain the high efficiency of TiO_2@Pt, as they enable rapid extraction and utilization of photoexcited electrons localized on Pt sites. In contrast, g-C_3N_4 is intrinsically visible-light active and readily generates photocarriers that can be intercepted by Pt. Upon Pt loading, electrons in the g-C_3N_4 conduction band transfer ultrafast to Pt nanoparticles, suppressing radiative recombination, as confirmed by steady-state PL quenching, shortened TCSPC lifetimes, and XPS-derived band energetics. EPR measurements under illumination reveal substantial enhancement of superoxide-related radical signals in Pt-modified g-C_3N_4, showing that Pt acts as an effective electron trap and initiates O_2 activation via the Pt^0/Pt^{2+} redox pair. It should be noted that these EPR measurements were performed on solid-state photocatalyst powders and serve to identify light-induced paramagnetic species on the catalyst surface, rather than to probe reaction intermediates formed during BPA degradation. These interfacial processes directly translate into improved BPA degradation efficiencies for CN-L@Pt and CN-H@Pt compared to their pristine counterparts. A notable performance difference arises between the two g-C_3N_4 supports. CN-H@Pt consistently surpasses CN-L@Pt in BPA degradation and mineralization, reflecting a combination of favourable textural, electronic, and interfacial factors. CN-H provides a significantly larger accessible surface area, facilitating better pollutant adsorption and more extensive Pt-support contact. TEM analyses show that CN-H stabilizes much smaller Pt nanoparticles (1.5 nm) compared to CN-L (3 nm), a behaviour rooted in its more negative zeta potential and higher density of deprotonated nitrogen sites during Pt deposition. Electrochemical measurements corroborate these trends as CN-H@Pt exhibits markedly lower charge-transfer resistance and higher photocurrent density, indicating more efficient charge separation and faster electron extraction than CN-L@Pt. XPS band-edge analysis further reveals that CN-H@Pt possesses a much smaller Schottky barrier height (0.26 eV) than CN-L@Pt (1.19 eV), enabling far more energetically favourable electron injection into Pt and correspondingly more effective O_2 activation. The more condensed heptazine structure of CN-H, characterized by fewer deep-trap defects, further contributes to the superior utilization of photogenerated carriers. In addition to BPA disappearance, the extent of carbon mineralization was evaluated by total organic carbon (TOC) analysis (Fig. 6b). The TOC data distinguish between mineralized carbon converted to CO_2 (TOC_M) and carbon retained in partially oxidized BPA-derived species adsorbed on the catalyst surface after reaction (TOC_A). Although nearly complete BPA removal is achieved with the most active photocatalysts, complete mineralization is not attained under visible-light irradiation, as indicated by the non-zero TOC_A fraction. Notably, for TiO_2@Pt and CN-H@Pt, the main contribution to TOC removal comes from TOC_M, indicating efficient deep oxidation rather than mere transformation of BPA into stable soluble by-products. The presence of surface-associated carbon species is characteristic of heterogeneous photocatalytic systems and suggests that these intermediates may undergo further oxidation with prolonged irradiation. To further identify the dominant reactive oxygen species involved in BPA degradation, additional ROS scavenger experiments were conducted under visible-light irradiation ($\lambda > 410$ nm) for TiO_2@Pt and CN-H@Pt (Fig. S16). For TiO_2@Pt, the presence of p-benzoquinone (BQ) causes a pronounced inhibition of BPA degradation, while tert-butanol (t-BuOH) results in a moderate decrease in activity, and formic acid (HCOOH) and sodium azide (NaN_3) have only minor effects. It should be noted that BQ may also act as a competitive electron acceptor in addition to scavenging superoxide radicals; therefore, the inhibition trends are interpreted within the broader mechanistic framework established in this work, rather than as standalone evidence for exclusive superoxide participation. This indicates that superoxide radicals play a dominant role in BPA degradation over TiO_2@Pt, with a secondary contribution from hydroxyl radicals, whereas photogenerated holes and singlet oxygen contribute negligibly under the applied conditions. In contrast, for CN-H@Pt, the strongest inhibition is observed with the addition of HCOOH, followed by BQ, while t-BuOH and NaN_3 cause only minor changes. This behaviour demonstrates that BPA degradation over CN-H@Pt is mainly governed by photogenerated holes and superoxide radicals, with hydroxyl radicals contributing weakly and singlet oxygen playing a negligible role. Finally, the operational stability of selected Pt-modified photocatalysts was evaluated through consecutive recycling experiments during the visible-light degradation of BPA. The representative catalysts CN-H@Pt and TiO_2@Pt exhibited stable photocatalytic performance over five successive cycles, with no noticeable loss of activity and essentially unchanged TOC removal efficiency, confirming good catalyst robustness under the investigated reaction conditions (Figs. S17 and S18).

To further clarify how Pt-support interactions influence ROS selectivity under visible-light illumination, we next use complementary $ABTS^{\bullet+}$ oxidation and coumarin hydroxylation assays, enabling us to map the ROS landscape of each photocatalyst and relate it to the interfacial electronic structure established above (Fig. 7). These observations indicate that the enhanced visible-light activity of the Pt-modified photocatalysts results from support-dependent redistribution of photogenerated charge carriers and Pt-mediated redox processes, rather than a universal increase in oxidative strength. The hydroxylation of coumarin into 7-hydroxycoumarin (7-HCOU) provides a direct probe for the formation of hydroxyl radicals under visible-light irradiation, enabling a clear mechanistic distinction between catalysts whose oxidative chemistry originates from semiconductor valence-band holes and those in which Pt itself acts as the active photo-responsive component (Fig. 7). Because TiO_2 does not absorb visible-light, the observed formation of 7-HCOU for TiO_2@Pt cannot stem from TiO_2 band-gap excitation. Instead, it can be attributed primarily to Pt-centered

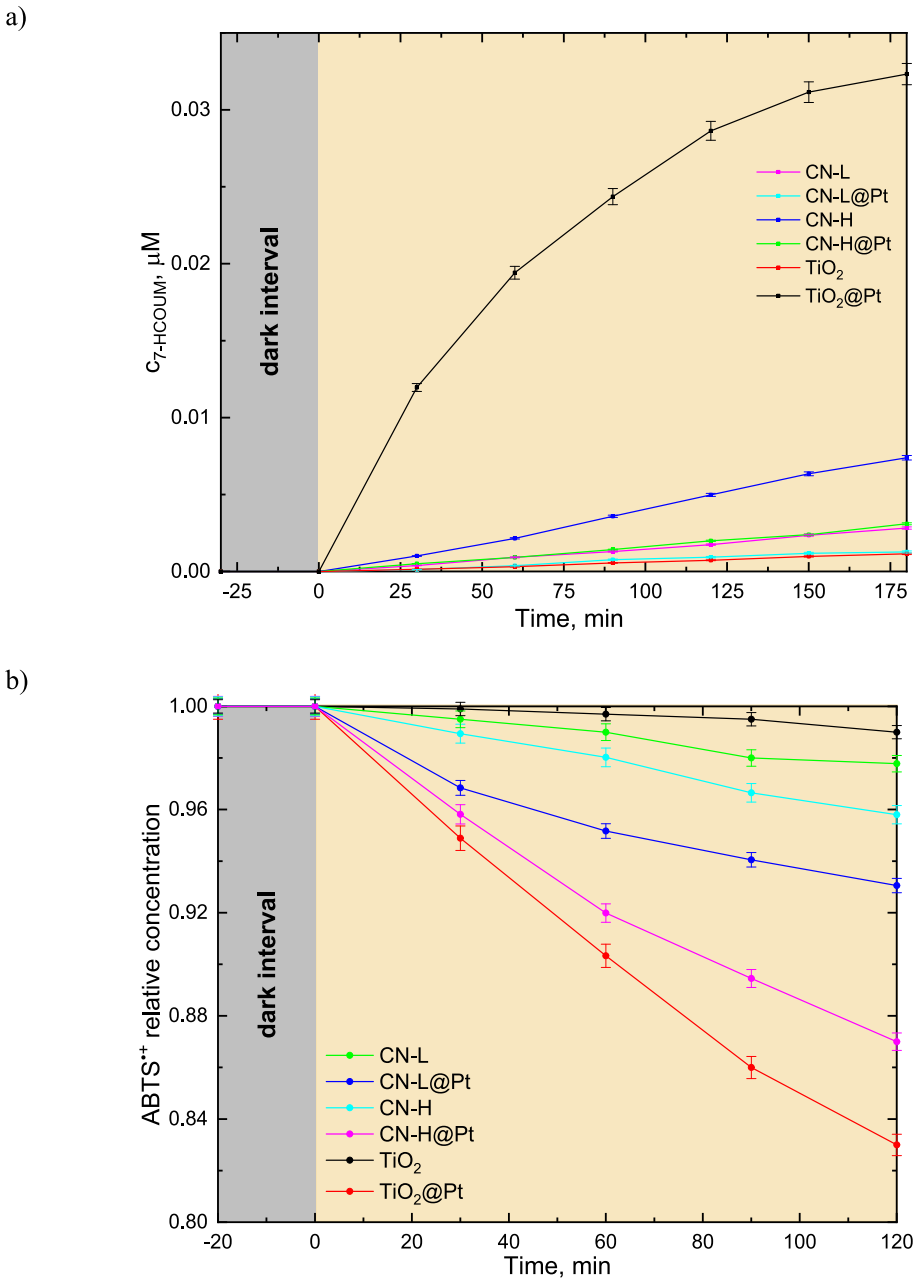

Fig. 7. a) Formation of 7-hydroxycoumarin (7-HCOUM) over time, and b) evolution of the normalized concentration of $ABTS^{\bullet+}$ during visible-light irradiation in the presence of the investigated photocatalysts (Schott KL 2500 LED source; emission profile shown in Fig. S1). Error bars represent ± standard deviation from three independent experiments.

oxidation pathways enabled by visible-light absorption on Pt. These pathways likely involve intra-band excitation or ligand-to-metal charge-transfer processes at the Pt/water interface, which generate highly oxidative Pt^{2+}/Pt^0 redox species capable of producing $OH^{\bullet}$. The measurable 7-HCOU signal for TiO_2@Pt therefore reflects Pt-driven radical formation, fully consistent with the absence of any visible-light-induced photocarrier signatures in TiO_2, as evidenced by the lack of PL, TCSPC, and EPR response. The behaviour of the carbon nitride systems differs fundamentally because g-C_3N_4 is intrinsically photo-active in the visible region and can generate holes energetic enough to oxidize water or surface hydroxyl groups to $OH^{\bullet}$. Pristine CN-H produces more 7-HCOU than CN-L, which reflects its more condensed heptazine framework and reduced density of deep-trap states that would otherwise consume photogenerated holes non-radiatively. After Pt deposition, however, both carbon nitride samples exhibit a decrease in 7-HCOU formation. This reduction is a direct consequence of the strong electron-sink function of Pt, which rapidly withdraws electrons from the g-C_3N_4 conduction band and thereby reduces the steady-state hole population available for hydroxyl radical formation. In both CN-L@Pt and CN-H@Pt, this redistribution of photogenerated charge away from the valence band suppresses hole-driven oxidation pathways and shifts the system towards alternative ROS-generating mechanisms. Although CN-H retains slightly higher $OH^{\bullet}$ generation than CN-L due to its more favourable electronic structure, Pt reduces hydroxyl radical formation to a comparable relative extent in both materials. This shared trend demonstrates that Pt deposition does not enhance $OH^{\bullet}$ production on g-C_3N_4 but instead competes with the intrinsic oxidative pathway by providing a fast, non-radiative electron-transfer channel that diminishes the availability of oxidative holes. These results align with the photocurrent, TCSPC, and PL analyses, all of which show accelerated charge

separation and reduced radiative recombination upon Pt incorporation, but with fewer holes remaining to drive $OH^{\bullet}$ chemistry. It should be emphasized that the applied ROS probe reactions selectively report on different oxidative pathways and do not provide a complete inventory of all transient reactive species present under illumination. The observed trends therefore reflect dominant, support-dependent reaction channels rather than exclusive ROS formation mechanisms.

The oxidation of $ABTS^{\bullet+}$ cation to ABTS provides a selective probe for one-electron oxidative pathways and thus offers complementary mechanistic insight to the coumarin test. Unlike hydroxyl radical formation, which requires strongly oxidizing valence-band holes, $ABTS^{\bullet+}$ oxidation can proceed via milder oxidative species or through direct electron transfer to Pt. Under visible-light irradiation, the photocatalysts investigated display markedly different ABTS generation behaviours, reflecting their distinct charge-transfer characteristics and their ability to stabilize reactive surface redox intermediates. TiO_2, which is not photoactive in the visible range, produces negligible ABTS in its pristine form, confirming that no photogenerated holes or electrons are created in the TiO_2 lattice under these conditions. After Pt deposition, however, TiO_2@Pt exhibits a clear and measurable ABTS signal. As TiO_2 cannot supply photogenerated carriers under visible-light, this activity must arise exclusively from Pt-centered one-electron oxidation pathways. Visible-light excitation of Pt nanoparticles leads to transient populations of hot carriers or ligand-to-metal charge-transfer states that are sufficiently oxidizing to abstract an electron from $ABTS^{\bullet+}$, forming ABTS. The low Schottky barrier at the Pt/TiO_2 interface facilitates rapid electron localization on Pt, effectively isolating Pt as the only reactive photoabsorbing site in the system. The $ABTS^{\bullet+}$ oxidation data therefore reaffirm that Pt is solely responsible for ROS initiation on TiO_2@Pt under visible-light, consistent with conclusions drawn from coumarin, PL, and EPR measurements. In contrast, the g-C_3N_4 samples display significant ABTS generation even in their pristine forms, reflecting their intrinsic visible-light activity and the ability of valence-band holes to drive single-electron oxidation reactions. The introduction of Pt dramatically enhances ABTS formation for both CN-L and CN-H, in stark contrast to the behaviour observed in the coumarin test. This strong increase demonstrates that Pt promotes one-electron oxidation pathways on g-C_3N_4, even though it suppresses hole-driven $OH^{\bullet}$ formation. The mechanistic origin of this enhancement lies in the redistribution of photogenerated charges. Pt efficiently extracts electrons from the g-C_3N_4 conduction band, increasing the lifetime and mobility of valence-band holes that remain available for milder oxidative reactions such as $ABTS^{\bullet+}$ oxidation. Unlike hydroxyl radical formation, which requires very high oxidation potentials, $ABTS^{\bullet+}$ oxidation proceeds readily even with partially stabilized holes or Pt-centered oxidants. Furthermore, the stronger ABTS signal observed for CN-H@Pt compared to CN-L@Pt reflects the more favourable electronic and structural properties of CN-H. Its smaller Pt nanoparticles, lower Schottky barrier height, and higher degree of polymerization collectively enable more efficient charge separation and a larger steady-state population of oxidative species, which accelerates $ABTS\bullet^{+}$ oxidation. In CN-L@Pt, the presence of deep-trap defects and larger Pt domains reduces the number of accessible oxidative carriers, resulting in lower ABTS formation.

Taken together, the photocatalytic degradation experiments reveal a consistent activity trend under visible-light irradiation: TiO_2@Pt > CN-H@Pt > CN-L@Pt > > pristine materials. CN-H@Pt generates reactive oxygen species more efficiently and achieves deeper BPA mineralization than CN-L@Pt, despite identical Pt loadings, demonstrating that performance is governed not by Pt content but by the support's ability to dictate the electronic behaviour of Pt. The combined influence of Pt nanoparticle size, Schottky barrier height, zeta potential-controlled nucleation, interfacial charge-transfer kinetics, and photocarrier dynamics explains the superior reactivity of CN-H@Pt and the more limited activity of CN-L@Pt, reflecting a direct correlation between the physicochemical properties of the support and the functionality of Pt at the interface. However, because BPA degradation integrates multiple oxidative pathways, it does not directly reveal which reactive oxygen species dominate on each catalyst. The coumarin and $ABTS^{\bullet+}$ assays therefore provide critical mechanistic insight. The coumarin data show that TiO_2@Pt generates $OH^{\bullet}$ exclusively through Pt-mediated oxidation under visible-light, consistent with the fact that TiO_2 itself is not photoactive in this spectral region. In contrast, both CN-L@Pt and CN-H@Pt produce fewer hydroxyl radicals than their pristine counterparts, demonstrating that Pt suppresses hole-driven $OH^{\bullet}$ formation on g-C_3N_4 by rapidly extracting electrons and lowering the steady-state concentration of valence-band holes. Viewed alongside the BPA results, this clearly indicates that $OH^{\bullet}$ is not the dominant ROS responsible for the enhanced photocatalytic performance of Pt-modified TiO_2 or g-C_3N_4. The $ABTS^{\bullet+}$ measurements reveal the complementary part of the ROS landscape. In sharp contrast to the coumarin test, $ABTS^{\bullet+}$ oxidation is strongly enhanced upon Pt deposition on both semiconductors, demonstrating that Pt shifts the ROS profile of g-C_3N_4 away from highly oxidative, hole-mediated radical chemistry towards more selective one-electron oxidation pathways. TiO_2@Pt again follows the same behaviour: because TiO_2 cannot generate photocarriers under visible-light, all ABTS formation originates from Pt-based photoexcitation and electron-transfer processes, confirming that Pt alone governs visible-light reactivity on the oxide support. Together, the coumarin and $ABTS^{\bullet+}$ tests reveal that Pt serves as the dominant mediator of ROS formation under visible-light irradiation, but the surrounding semiconductor determines which ROS pathways are accessible. On TiO_2, Pt drives both $OH^{\bullet}$ and one-electron oxidation exclusively through its own photophysics. On g-C_3N_4, Pt suppresses hydroxyl radical formation while simultaneously enhancing ABTS production, redirecting the reaction chemistry towards milder oxidative pathways that nevertheless yield higher BPA mineralization efficiency. This mechanistic behaviour underscores the central conclusion of the study, namely that the semiconductor support controls not only the electronic state and reactivity of Pt, but also the distribution of reactive oxygen species generated under illumination, thereby dictating the efficiency and selectivity of photocatalytic processes.

The enhancement of photocatalytic performance induced by Pt nanoparticles results from their support-dependent electronic role, rather than direct participation as independent catalytic centers. Under visible-light irradiation, charge carriers are generated either in the semiconductor support (g-C_3N_4) or via Pt-mediated sub-band-gap excitation pathways. In both cases, Pt nanoparticles serve as energetically favourable electron sinks, promoting rapid interfacial charge transfer, suppressing electron-hole recombination, and extending the lifetime of reactive charge carriers at the semiconductor surface. This behaviour is demonstrated by pronounced PL quenching, shortened lifetimes in TCSPC, enhanced photocurrent responses, and reduced charge-transfer resistance. In TiO_2-based systems, Pt enables efficient visible-light-driven oxygen activation and superoxide formation through interfacial electron trapping, while maintaining the strong oxidative potential of the TiO_2 valence band. In contrast, in g-C_3N_4-based systems, stronger electronic coupling between Pt and the polymeric framework leads to enhanced charge separation and band bending effects, favouring hole-driven oxidation and selective one-electron oxygen reduction pathways. Consequently, Pt nanoparticles function as electronic regulators that modulate charge-carrier dynamics and ROS selectivity according to the intrinsic electronic structure of the support, thereby directly enhancing photocatalytic activity.

3.5. H_2-assisted thermal and light-driven photothermal reduction of NO_2

The temperature-dependent NO_2 reduction experiments conducted in the dark (Fig. 8a) show that the bare supports (TiO_2, CN-L, CN-H) are essentially inactive within the investigated temperature range, whereas Pt deposition immediately enables measurable NO_2 conversion. This behaviour is fully consistent with previous studies on Pt/TiO_2 systems, where bare TiO_2 did not catalyze H_2-assisted NO_2 reduction between 30 and 400 °C, while the presence of Pt activated the deNO_2 process and

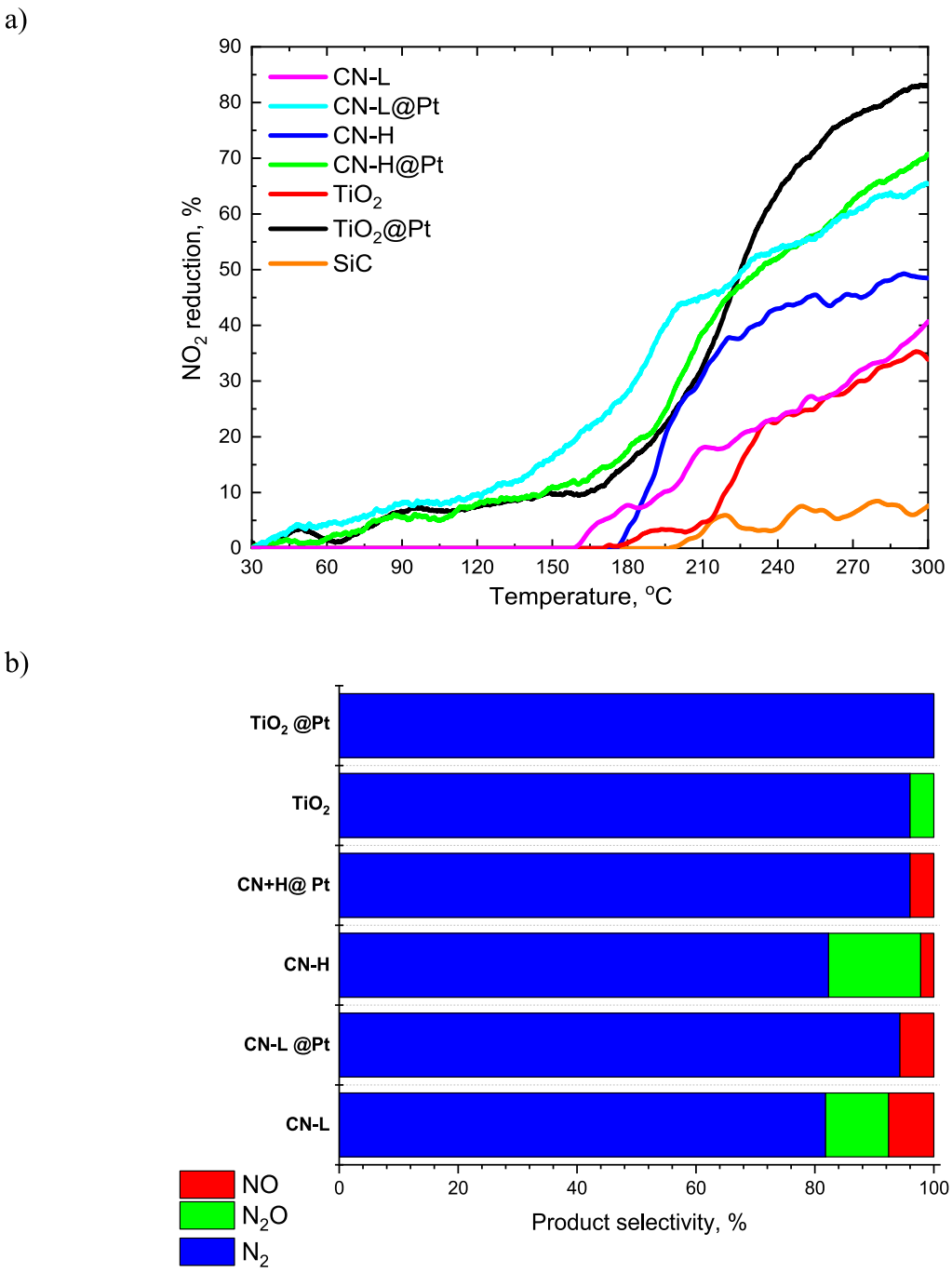

Fig. 8. a) Temperature-dependent relative NO_2 conversion over pure TiO_2, pure CNs, and the TiO_2@Pt and CN@Pt catalysts. The SiC trace corresponds to an inert reference experiment conducted under identical reaction conditions, confirming the absence of non-catalytic NO_2 conversion. b) Relative percentage selectivity of the three primary products (NO, N_2O, and N_2) calculated within the temperature range of 30–300 °C for the studied materials.

shifted the ignition temperature into the low-intermediate range [15,16]. In our case, all Pt-modified materials exhibit a gradual increase in NO_2 conversion with temperature, confirming that Pt provides the primary active sites for NO_2 adsorption, dissociation, and subsequent reduction, while the support mainly tunes the dispersion, redox properties, and electronic environment of the Pt phase. A clear activity trend emerges among the Pt-containing catalysts, following the order TiO_2@Pt > CN-H@Pt > CN-L@Pt. This ranking directly reflects the interplay between Pt dispersion, support textural properties, and Pt-support electronic coupling. TEM and STEM-EDXS analyses show that TiO_2@Pt contains the smallest and most narrowly distributed Pt nanoparticles, whereas CN-H@Pt stabilizes slightly larger particles, and CN-L@Pt features significantly coarser Pt aggregates. Smaller Pt particles expose more low-coordinated sites and metal-support interfacial regions, which are particularly active for NO_2 activation and hydrogenation of NO_x intermediates. This trend matches the behaviour reported for TiO_2 + Pt catalysts in the reference system, where the catalyst with the highest dispersion of small Pt particles exhibited the best low-temperature NO_2 reduction performance [15,16]. Beyond morphology, the support also controls the electronic structure at the metal-support junction. XPS band-edge analysis and valence-band measurements show that the SBH at the Pt/semiconductor interface decreases in the order CN-L@Pt (1.19 eV) > CN-H@Pt (0.26 eV) > TiO_2@Pt (0.16 eV). Although NO_2 reduction in the dark is driven

thermally rather than photochemically, SBH still governs the equilibrium distribution of electrons between Pt and the support, and thus the redox state and electron density on Pt. A lower SBH favours electron accumulation on Pt at a given Fermi level, which facilitates electron transfer into adsorbed NO_2 and NO_x intermediates. This provides a natural explanation for the observed activity order. TiO_2@Pt, with the lowest SBH and the smallest Pt particles, exhibits the earliest onset of NO_2 conversion and the highest overall activity, while CN-H@Pt, with intermediate SBH and moderately small Pt nanoparticles, shows improved performance over CN-L@Pt but does not reach the activity of TiO_2@Pt. Finally, CN-L@Pt, characterized by the highest SBH and the largest Pt aggregates, displays the weakest thermocatalytic response. The selectivity analysis (Fig. 8b) further supports the conclusion that Pt is the main active phase and that the support primarily modulates its kinetics rather than altering the fundamental reaction pathway. In analogy with previously studied TiO_2 + Pt catalysts [15,16], where all materials exhibited very high selectivity towards N_2 formation (>97%), our Pt-modified catalysts produce predominantly N_2, with NO and N_2O remaining minor by-products over the entire temperature range. This indicates that, once NO_2 is activated on Pt, the sequence of elementary steps (NO_2 adsorption, reduction to NO and surface nitrite/nitrate species, followed by further hydrogenation and recombination to N_2) proceeds efficiently on all Pt surfaces. Differences between TiO_2@Pt, CN-H@Pt and CN-L@Pt therefore arise mainly from how easily these pathways are initiated (ignition temperature, apparent rate), which in turn is dictated by Pt particle size, support reducibility, and Pt-support interaction strength, in line with conclusions drawn for TiO_2 + Pt catalysts in the literature [15,16]. The dark NO_2 reduction experiments demonstrate that thermocatalytic activity is not controlled by Pt loading alone, but rather by how the support regulates Pt dispersion, oxidation state, and electronic environment. TiO_2, with its high surface area, strong metal-oxide interactions, and low SBH, provides the most favourable platform for Pt-mediated NO_2 reduction, while CN-H offers an intermediate case where improved textural properties and lower SBH lead to a clear enhancement over CN-L. These thermocatalytic trends provide a crucial reference point for the subsequent analysis of visible-light and photothermal NO_2 reduction, where additional photoinduced charge carriers and plasmon-like Pt excitations come into play and further amplify the role of the support in governing Pt reactivity.

Fig. 9 illustrates how the catalytic behaviour of Pt-modified TiO_2 and g-C_3N_4 changes when visible-light irradiation is applied after the catalyst has reached its thermal steady state. In this experimental design, illumination does not initiate the reaction but perturbs an already active thermocatalytic system, allowing the separation of purely photonic contributions from classical temperature-driven kinetics. Consequently, the response observed in Fig. 9 reflects genuine photothermal modulation of an established catalytic landscape, rather than a shift in the ignition mechanism as seen in Fig. 8. Under dark conditions, the temperature dependence follows the same hierarchy established in Fig. 8 (TiO_2@Pt > CN-H@Pt > CN-L@Pt), confirming that Pt dispersion, particle size, and Schottky barrier height determine the intrinsic thermocatalytic kinetics. However, once the system is illuminated at the target temperature, the reaction dynamics change abruptly, depending on both the optical properties of the support and the electronic accessibility of Pt. Because illumination is applied at constant temperature, the observed increases in NO_2 conversion cannot be attributed to thermal activation alone. Instead, they reflect the ability of visible-light to inject nonequilibrium carriers or generate localized photothermal fields that perturb the electronic structure of the Pt-support interface. The strongest illumination-induced enhancement occurs at low and intermediate temperatures, where the dark reaction is still limited by the availability of reducing electrons at the Pt surface. In TiO_2@Pt, where TiO_2 does not absorb visible-light, this enhancement must arise from Pt itself. The light-induced promotion of NO_2 conversion is therefore attributed to Pt-centered electronic excitation (hot-carrier formation and sub-bandgap photothermal heating) superimposed on the pre-existing thermal reaction. Because the system has already reached thermal equilibrium before illumination, the magnitude of the photocatalytic "jump" directly reflects the efficiency with which Pt can transiently deepen its reducing chemical potential under visible-light excitation. The narrow Pt particle size distribution and ultralow SB in TiO_2@Pt amplify this effect, making it the most responsive catalyst

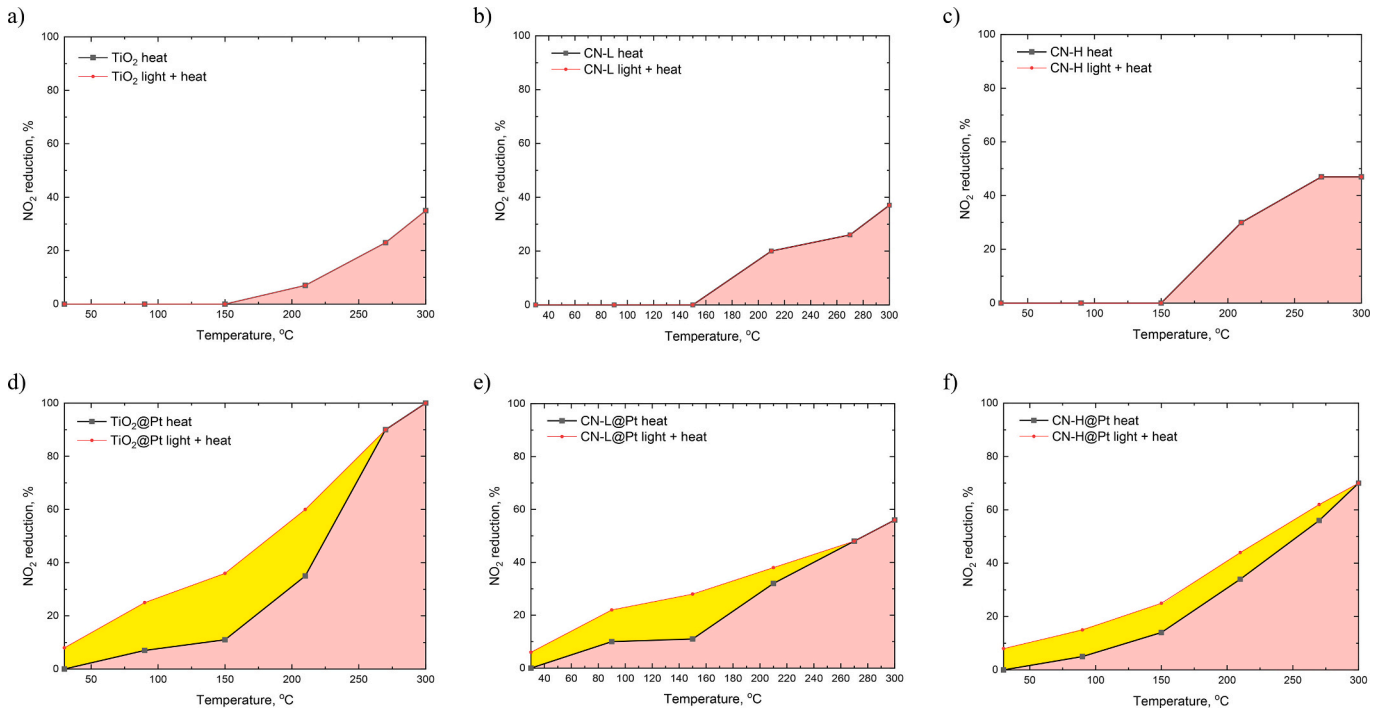

Fig. 9. Temperature-dependent NO_2 reduction curves under dark conditions (black curves) and under visible-light illumination (red curves) for pure TiO_2, pure CN, and TiO_2@Pt and CN@Pt catalysts.

under illumination. The CN-based materials exhibit a qualitatively different behaviour. Since g-C_3N_4 absorbs visible-light efficiently, illumination introduces an additional electron-flux channel into Pt that is not available in TiO_2@Pt. At fixed temperature, this charge injection increases electron residence time within the Pt surface and facilitates reduction steps that are thermally accessible but kinetically hindered in the dark. The difference between CN-H@Pt and CN-L@Pt mirrors their SBH values. CN-H@Pt, with its lower interfacial barrier and fewer recombination sites, shows a much sharper illumination-induced enhancement than CN-L@Pt. Because illumination is applied only after the catalyst has equilibrated thermally, the magnitude of this optical promotion provides a direct measure of how effectively each support can deliver and stabilize photogenerated carriers at Pt under steady-state reaction conditions. At elevated temperatures, illumination produces only marginal improvements, indicating that once the thermal barrier is sufficiently low, the reaction no longer depends on optically generated carriers. This collapse of the photocatalytic advantage at high temperatures emphasizes that illumination acts not as an alternative ignition mechanism but as an electronic perturbation superimposed on the existing thermal kinetics, and its impact is strongest where the dark reaction is most electron-limited. To summarize, Fig. 9 demonstrates that visible-light excitation modifies an already active thermocatalytic pathway, rather than substituting for thermal activation. The magnitude and character of this modification depend sensitively on the interfacial energetics between Pt and the support (particle size, SBH, and the support's optical response), revealing that light does not change the fundamental mechanism of NO_2 reduction but instead shifts the kinetic balance by altering electron availability at the Pt surface. This mechanistic distinction, enabled only by the "heat-then-illuminate" experimental design, provides a unique window into how photothermal and photochemical effects integrate with classical heterogeneous catalysis.

4. Conclusions

This study demonstrates that the catalytic function of Pt NPs cocatalysts in semiconductor-based photocatalysts is strongly governed by the electronic properties of the supporting material, rather than by Pt loading or surface accessibility alone. By deliberately matching the textural properties of TiO_2 and g-C_3N_4 supports and applying an identical Pt NPs deposition protocol, support-induced effects on interfacial energetics, charge-transfer behaviour, and reactive oxygen species (ROS) pathways could be isolated with minimal geometric bias.

The results show that TiO_2 stabilizes predominantly metallic Pt nanoparticles and forms a low effective Schottky barrier, enabling rapid electron extraction and Pt-centered visible-light activity that promotes both hydroxyl radical formation and efficient thermocatalytic NO_2 reduction. In contrast, g-C_3N_4 induces pronounced band bending and stabilizes mixed Pt^0/Pt^{2+} states, leading to higher interfacial barriers, suppressed hydroxyl radical generation, and preferential activation of one-electron oxidation pathways. These differences persist even when TiO_2 and high-surface-area g-C_3N_4 have comparable surface areas, confirming that Pt functionality is electronically programmed by the support rather than dictated by surface exposure alone.

Importantly, the redistribution of photogenerated charge carriers caused by Pt loading does not universally enhance oxidative strength but instead redirects the ROS landscape in a support-dependent manner. While Pt enhances visible-light activity on TiO_2 primarily through Pt-centered excitation processes, its role on g-C_3N_4 is to selectively extract electrons, suppress hole-driven hydroxyl radical formation, and promote milder yet highly effective one-electron oxidation pathways.

In this context, the semiconductor support does not merely host Pt NPs but actively programmes their electronic structure, charge-transfer behaviour, and catalytic role. Taken together, these findings highlight that noble-metal cocatalysts cannot be regarded as electronically universal components in photocatalytic systems. Instead, their function emerges from the interplay between metal electronic structure, semiconductor band alignment, and interfacial charge-transfer kinetics. This insight provides a rational framework for the deliberate design of Pt-based photocatalysts in which the semiconductor support is used as an active parameter to control cocatalyst functionality, ROS selectivity, and overall catalytic performance.

CRediT authorship contribution statement

Gregor Žerjav: Writing – review & editing, Writing – original draft, Validation, Supervision, Investigation, Conceptualization. **Andraž Mavrič:** Writing – review & editing, Visualization, Investigation. **Miklós Németh:** Writing – review & editing, Investigation. **Albin Pintar:** Writing – review & editing, Validation, Investigation, Funding acquisition, Data curation.

Declaration of competing interest

The authors declare that they have no known competing financial interests or personal relationships that could have appeared to influence the work reported in this paper.

Acknowledgements

The authors would like to express their gratitude to the Slovenian Research and Innovation Agency for providing financial support through research core funding under grants P2-0150 and P2-0412.

Appendix A. Supplementary data

Supplementary data to this article can be found online at https://doi.org/10.1016/j.cej.2026.174635.

Data availability

Data will be made available on request.

References

[1] D. Krishan, D. Yadav, A. Srivastava, Water pollution's global threat to public health: a mini-review, Int. J. Sci. Res. Eng. Technol. 6 (2023) (2023) 321–334, https://doi.org/10.32628/ijsrset2310643.
[2] R.P. Schwarzenbach, T. Egli, B. Wehrli, T.B. Hofstetter, U. Von Gunten, Global water pollution and human health, Annu. Rev. Environ. Resour. 35 (2010) 109–136, https://doi.org/10.1146/annurev-environ-100809-125342.
[3] C. Di Marcantonio, F. Mangiagli, M. Rosaria Boni, J. Bartolucci, S. Bongirolami, R. Romano, A. Martelli, D. Rapinesi, F. Altobelli, Agostina Chiavola, Are we ready for the application of the EU Regulation on wastewater reuse in agriculture? A techno-economic preliminary evaluation based on a case-study, J. Environ. Manag. 373 (2025) 123973, https://doi.org/10.1016/j.jenvman.2024.123973.
[4] A. Mohamed, S. Yousef, W.S. Nasser, T.A. Osman, A. Knebel, E.P.V. Sánchez, T. Hashem, Rapid photocatalytic degradation of phenol from water using composite nanofibers under UV, Environ. Sci. Eur. 32 (2020), https://doi.org/10.1186/S12302-020-00436-0.
[5] Y. Jari, N. Najid, M.C. Necibi, B. Gourich, C. Vial, A. Elhalil, P. Kaur, I. Mohdeb, Y. Park, Y. Hwang, A. Ruiz Garcia, N. Roche, A. El Midaoui, A comprehensive review on TiO_2-based heterogeneous photocatalytic technologies for emerging pollutants removal from water and wastewater: From engineering aspects to modeling approaches, J. Environ. Manag. 373 (2025) 123703, https://doi.org/10.1016/j.jenvman.2024.123703.
[6] G. Žerjav, J. Zavašnik, J. Kovač, A. Pintar, The influence of Schottky barrier height onto visible-light triggered photocatalytic activity of TiO_2 + Au composites, Appl. Surf. Sci. 543 (2021) 148799, https://doi.org/10.1016/j.apsusc.2020.148799.
[7] M. Raaja Rajeshwari, S. Kokilavani, S. Sudheer Khan, Recent developments in architecturing the g-C_3N_4 based nanostructured photocatalysts: Synthesis, modifications and applications in water treatment, MDPI, Chemosphere 291 (2022) 132735, https://doi.org/10.1016/j.chemosphere.2021.132735.
[8] S. Abou Zeid, Y. Leprince-Wang, Advancements in ZnO-based photocatalysts for water treatment: a comprehensive review, MDPI Crystals 14 (2024) 611, https://doi.org/10.3390/cryst14070611.
[9] C. Lykos, F. Bairamis, C. Efthymiou, I. Konstantinou, Synthesis and characterization of composite WO_3 fibers/g-C_3N_4 photocatalysts for the removal of the insecticide clothianidin in aquatic media, MDPI Nanomater. 14 (2024) 1045, https://doi.org/10.3390/nano14121045.

[10] X. Hao, J. Zhou, Z. Cui, Y. Wang, Y. Wang, Z. Zou, Zn-vacancy mediated electron-hole separation in ZnS/g-C_3N_4 heterojunction for efficient visible-light photocatalytic hydrogen production, Appl. Catal. B Environ. 229 (2018) 41–51, https://doi.org/10.1016/j.apcatb.2018.02.006.

[11] S.J. Mun, S.-J. Park, Graphitic carbon nitride materials for photocatalytic hydrogen production via water splitting: a short review, MDPI Catalysts 9 (2019) 805, https://doi.org/10.3390/catal9100805.

[12] C. Acar, G.F. Naterer, I. Dincer, Review of photocatalytic water-splitting methods for sustainable hydrogen production, Int. J. Energy Res. 40 (2016) 1449–1473, https://doi.org/10.1002/er.3549.

[13] Y. Zhu, J. Li, J. Cao, C. Lv, G. Huang, G. Zhang, Y. Xu, S. Zhang, P. Meng, T. Zhan, D. Yang, Phosphorus-doped polymeric carbon nitride nanosheets for enhanced photocatalytic hydrogen production, APL Mater. 8 (2020) 041108, https://doi.org/10.1063/1.5143711.

[14] M. Ismael, A review on graphitic carbon nitride (g-C_3N_4) based nanocomposites: Synthesis, categories, and their application in photocatalysis, J. Alloys Compd. 846 (2020) 156446, https://doi.org/10.1016/j.jallcom.2020.156446.

[15] G. Žerjav, Z. Say, J. Zavašnik, M. Finšgar, C. Langhammer, A. Pintar, Photo, thermal and photothermal activity of TiO_2 supported Pt catalysts for plasmon-driven environmental applications, J. Environ. Chem. Eng. 11 (2023) 110209, https://doi.org/10.1016/j.jece.2023.110209.

[16] G. Žerjav, J. Zavašnik, M. Roškarič, M. Finšgar, A. Beck, A. Horváth, A. Pintar, Photothermal catalytic properties of TiO_2+Pt solids: A multifunctional approach to environmental remediation, J. Environ. Chem. Eng. 13 (2025) 117576, https://doi.org/10.1016/j.jece.2025.117576.

[17] A.P. Devi, D.K. Padhi, P.M. Mishra, A.K. Behera, Bio-surfactant mediated synthesis of Au/g-C_3N_4 plasmonic hybrid nanocomposite for enhanced photocatalytic reduction of mono-nitrophenols, J. Ind. Eng. Chem. 108 (2022) 118–129, https://doi.org/10.1016/j.jiec.2021.12.030.

[18] F. Ding, T. Ming, H. Zhang, Y. Gao, V. Dragutan, Y. Sun, I. Dragutan, Z. Xu, Plasmonic Ag nanoparticles decorated g-C_3N_4 for enhanced visible-light driven photocatalytic degradation and H_2 production, J. Rec. 1 (2022) 1–7, https://doi.org/10.1016/j.recm.2021.12.004.

[19] R. Zhang, J. Wang, P. Han, Highly efficient photocatalysts of Pt/BN/CdS constructed by using the Pt as the electron acceptor and the BN as the holes transfer for H_2-production, J. Alloys Compd. 637 (2015) 483–488, https://doi.org/10.1016/j.jallcom.2015.03.047.

[20] Y. He, Z. Ren, L. Yan, J. Liu, L.A. Belfiore, J. Tang, S. Mao, Pt nanoparticles enhanced TiO_2 on ultra-violet photo-detection: Hot-electron injection effect over near-field enhancement, Appl. Surf. Sci. 605 (2022) 154768, https://doi.org/10.1016/j.apsusc.2022.154768.

[21] I. Benisti, F. Shaik, Z. Xing, A. Ben-refael, L. Amirav, Y. Paz, The effect of Pt cocatalyst on the performance and transient IR spectrum of photocatalytic g-C_3N_4 nanospheres, Appl. Surf. Sci. 542 (2021) 148432, https://doi.org/10.1016/j.apsusc.2020.148432.

[22] M. Roškarič, G. Žerjav, M. Finšgar, J. Zavašnik, A. Pintar, Influence of the calcination duration of g-C_3N_4/TiO_2 "veggie-toast-like" photocatalyst on the visible-light triggered photocatalytic oxidation of bisphenol A, J. Alloys Compd. 947 (2023) 169585, https://doi.org/10.1016/j.jallcom.2023.169585.

[23] J. Wen, J. Xie, X.i Chen, X. Li, A review on g-C_3N_4-based photocatalysts, Appl. Surf. Sci. 391 (2017) 72–123, https://doi.org/10.1016/j.apsusc.2016.07.030.

[24] T.P. Yadav, J.L. Palma, D.P. Singh, S. Michea, Facile synthesis and magnetic behavior of 1D g-C_3N_4, J. Solid State Chem. 290 (2020) 121539, https://doi.org/10.1016/j.jssc.2020.121539.

[25] C. Hu, Z.-T. Liu, K.-Y. Andrew Lin, W.-H. Wei, K.-H. Wang, Synergistic effect of KCl mixing and melamine/urea mixture in the synthesis of g-C_3N_4 for photocatalytic removal of tetracycline, J. Ind. Eng. Chem. 107 (2022) 118–125, https://doi.org/10.1016/j.jiec.2021.11.036.

[26] Z. Zhang, Y. Zheng, J. Hang Xie, X. Zhao, W. Guo, Q. Zhang, S. Fu, Q. Wang, Y. Huang Xu, Synthesis of g-C_3N_4 microrods with superficial C, N dual vacancies for enhanced photocatalytic organic pollutant removal and H_2O_2 production, J. Alloys Compd. 904 (2022) 164028, https://doi.org/10.1016/j.jallcom.2022.164028.

[27] D. Shi, J. Liu, S. Ji, Preparation of Au/TiO_2 catalyst and the performance of liquid methanol catalytic oxidation to formic acid, Ind. Eng. Chem. Res. 56 (2017) 11028–11033, https://doi.org/10.1021/acs.iecr.7b02506.

[28] X. Zhu, E. Zhou, X. Tai, H. Zong, J. Yi, Z. Yuan, X. Zhao, P. Huang, H. Xu, Z. Jiang, g-C_3N_4 S-scheme homojunction through Van der Waals interface regulation by intrinsic polymerization tailoring for enhanced photocatalytic H_2 evolution and CO_2 reduction, Angew. Chem. Int. Ed. 64 (2025) e202425439, https://doi.org/10.1002/anie.202425439.

[29] M. Roškarič, J. Zavašnik, D. Zámbó, T. Kotnik, S. Kovačič, G. Žerjav, A. Pintar, Optimization method based on simplex for surface area improved photocatalytic performance of g-C_3N_4, ACS Catal. 13 (2023) 13282–13300, https://doi.org/10.1021/acscatal.3c03394.

[30] P. Xia, B. Cheng, J. Jiang, H. Tang, Localized π-conjugated structure and EPR investigation of g-C_3N_4 photocatalyst, Appl. Surf. Sci. 487 (2019) 335–342, https://doi.org/10.1016/j.apsusc.2019.05.064.

[31] Y. Li, R. He, P. Han, B. Hou, S. Peng, C. Ouyang, A new concept: volume photocatalysis for efficient H_2 generation - using low polymeric carbon nitride as an example, Appl. Catal. B 279 (2020) 119379, https://doi.org/10.1016/j.apcatb.2020.119379.

[32] S.R. Damkale, S.S. Arbuj, G.G. Umarji, S.B. Rane, B.B. Kale, Highly crystalline anatase TiO_2 nanocuboids as an efficient photocatalyst for hydrogen generation, RSC Adv. 11 (2021) 7587–7599, https://doi.org/10.1039/d0ra10750f.

[33] S. Yurdakal, C. Garlisi, L. Özcan, M. Bellardita, G. Palmisano, Heterogeneous photocatalysis chapter 4 - (photo)catalyst characterization techniques: adsorption isotherms and BET, SEM, FTIR, UV–Vis, photoluminescence, and electrochemical characterizations, 2019, pp. 87–152, https://doi.org/10.1016/B978-0-444-64015-4.00004-3.

[34] G. Žerjav, M. Roškarič, J. Zavašnik, J. Kovač, A. Pintar, Effect of Au loading on Schottky barrier height in TiO_2 + Au plasmonic photocatalysts, Appl. Surf. Sci. 579 (2022) 152196, https://doi.org/10.1016/j.apsusc.2021.152196.

[35] J.G. Yu, J.F. Xiong, B. Cheng, S.W. Liu, Fabrication and characterization of Ag-TiO_2 multiphase nanocomposite thin films with enhanced photocatalytic activity, Appl. Catal. B 60 (2005) 211–221, https://doi.org/10.1016/j.apcatb.2005.03.009.

[36] U. Diebold, T.E. Madey, TiO_2 by XPS, Surf. Sci. Spectra 4 (1996) 227–231, https://doi.org/10.1116/1.1247794.

[37] K. Bhattacharyya, A. Danon, B.K. Vijayan, K.A. Gray, P.C. Stair, E. Weitz, Role of the surface Lewis acid and base sites in the adsorption of CO_2 on titania nanotubes and platinized titania nanotubes: an in situ FT-IR study, J. Phys. Chem. C 117 (2013) 12661–12678, https://doi.org/10.1021/jp402979m.

[38] M. Seredych, S. Łoś, D.A. Giannakoudakis, E. Rodríguez-Castellón, T.J. Bandosz, Photoactivity of g-C_3N_4/S-Doped Porous Carbon Composite: Synergistic Effect of Composite Formation, ChemSusChem 9 (2016) 795–799, https://doi.org/10.1002/cssc.201501658.

[39] S. Zuluaga, L.-H. Liu, N. Shafiq, S.M. Rupich, J.-F. Veyan, Y.J. Chabalb, T. Thonhauser, Structural band-gap tuning in g-C_3N_4, Phys.Chem.Chem.Phys. 17 (2015) 957, https://doi.org/10.1039/c4cp05164e.

[40] J. Ma, F. Wang, M. Mostafavi, Ultrafast chemistry of water radical cation, $H_2O^{\bullet+}$, in aqueous solutions, MDPI Molecules 23 (2018) 244, https://doi.org/10.3390/molecules23020244.

[41] Y. Tian, L. Kong, H. Zou, M. Liu, G. Liu, Boosting hydroxyl radical generation for highly efficient electrooxidation of sulfamethazine via facile doping strategy, Sustainable Horiz. 11 (2024) 100103, https://doi.org/10.1016/j.horiz.2024.100103.

[42] G. Žerjav, K. Žižek, J. Zavašnik, A. Pintar, Brookite vs. rutile vs. anatase: what's behind their various photocatalytic activities? J. Environ. Chem. Eng. 10 (2022) 107722 https://doi.org/10.1016/j.jece.2022.107722.

[43] F. Xu, L. Zheng, J. Zhang, Y. He, H. Cao, X. Zheng, H. García, J. Yu, Co_3O_4 as full-solar-spectrum photocatalyst for selective methane conversion through reactive oxygen species control, Nat. Catal. 9 (2026) 73–86, https://doi.org/10.1038/s41929-025-01471-x.

[44] B. Choudhury, A. Choudhury, Oxygen defect dependent variation of band gap, Urbach energy and luminescence property of anatase, anatase-rutile mixed phase and of rutile phases of TiO_2 nanoparticles, Phys. E. 56 (2014) 364–371, https://doi.org/10.1016/j.physe.2013.10.014.

[45] H. Luo, Y. Liu, S.D. Dimitrov, L. Steier, S. Guo, X. Li, J. Feng, F. Xie, Y. Fang, A. Sapelkin, X. Wang, M.-M. Titirici, Pt single-atoms supported on nitrogen-doped carbon dots for highly efficient photocatalytic hydrogen generation, J. Mater. Chem. A 8 (2020) 14690–14696, https://doi.org/10.1039/D0TA04431H.

[46] H. Xu, X. Liu, G. Zhou, C. Bi, Q. Liu, W. Jiang, B. Wang, X. Zhu, P.K. Chu, X. Wang, Controlled photocatalytic reduction of CO_2 by precise atomic-level interface modification and engineering of silver nanoclusters, Adv. Sci. 13 (2026) e16096, https://doi.org/10.1002/advs.202516096.

[47] A.E. Giannakas, M. Antonopoulou, J. Papavasiliou, Y. Deligiannakis, I. Konstantinou, Photocatalytic performance of Pt-TiO_2, Pt-N-TiO_2 and Pt-N/F-TiO_2 towards simultaneous Cr(VI) reduction/benzoic acid oxidation: Insights into photogenerated charge carrier dynamics and catalyst properties, J. Photochem. Photobiol. A 349 (2017) 25–35, https://doi.org/10.1016/j.jphotochem.2017.08.066.

[48] M. Chiesa, M.C. Paganini, S. Livraghia, Elio Giamello, Charge trapping in TiO_2 polymorphs as seen by Electron Paramagnetic Resonance spectroscopy, Phys. Chem. Chem. Phys. 15 (2013) 9435–9447, https://doi.org/10.1039/C3CP50658D.

[49] C.P. Kumar, N.O. Gopal, T.C. Wang M.-S. Wong, S. Chu Ke, EPR Investigation of TiO_2 Nanoparticles with Temperature-Dependent Properties, J. Phys. Chem. 110 (2006) 5223–5229, https://doi.org/10.1021/jp057053t.

[50] S. Livraghi, M. Chiesa, M.C. Paganini, E. Giamello, On the nature of reduced states in titanium dioxide as monitored by electron paramagnetic resonance. I: The anatase case, J. Phys. Chem. C 115 (2011) 25413–25421, https://doi.org/10.1021/jp209075m.

[51] X. Chen, L. Liu, F. Huang, Black titanium dioxide (TiO_2) nanomaterial, Chem. Soc. Rev. 44 (2015) 1861–1885, https://doi.org/10.1039/C4CS00330F.

[52] Y. Lu, C. Liu, L. Zheng, F. Chen, J. Qian, X. Meng, Z. Chen, S. Zhong, B. He, N3C-defect-tuned g-C3N4 photocatalysts: structural optimization and enhanced tetracycline degradation performance, MDPI Nanomater. 15 (2025) 466, https://doi.org/10.3390/nano15060466.

[53] X. Bi, L.-Z. Wang, D.-H. Zhai, L. Wang, H. Yang, G.-H. Du, In-situ synthesis of g-C_3N_4 with nitrogen vacancy and cyano group via one-pot method for enhanced photocatalytic activity, Sci. Rep. 15 (2025) (2025) 19864, https://doi.org/10.1038/s41598-025-03286-z.